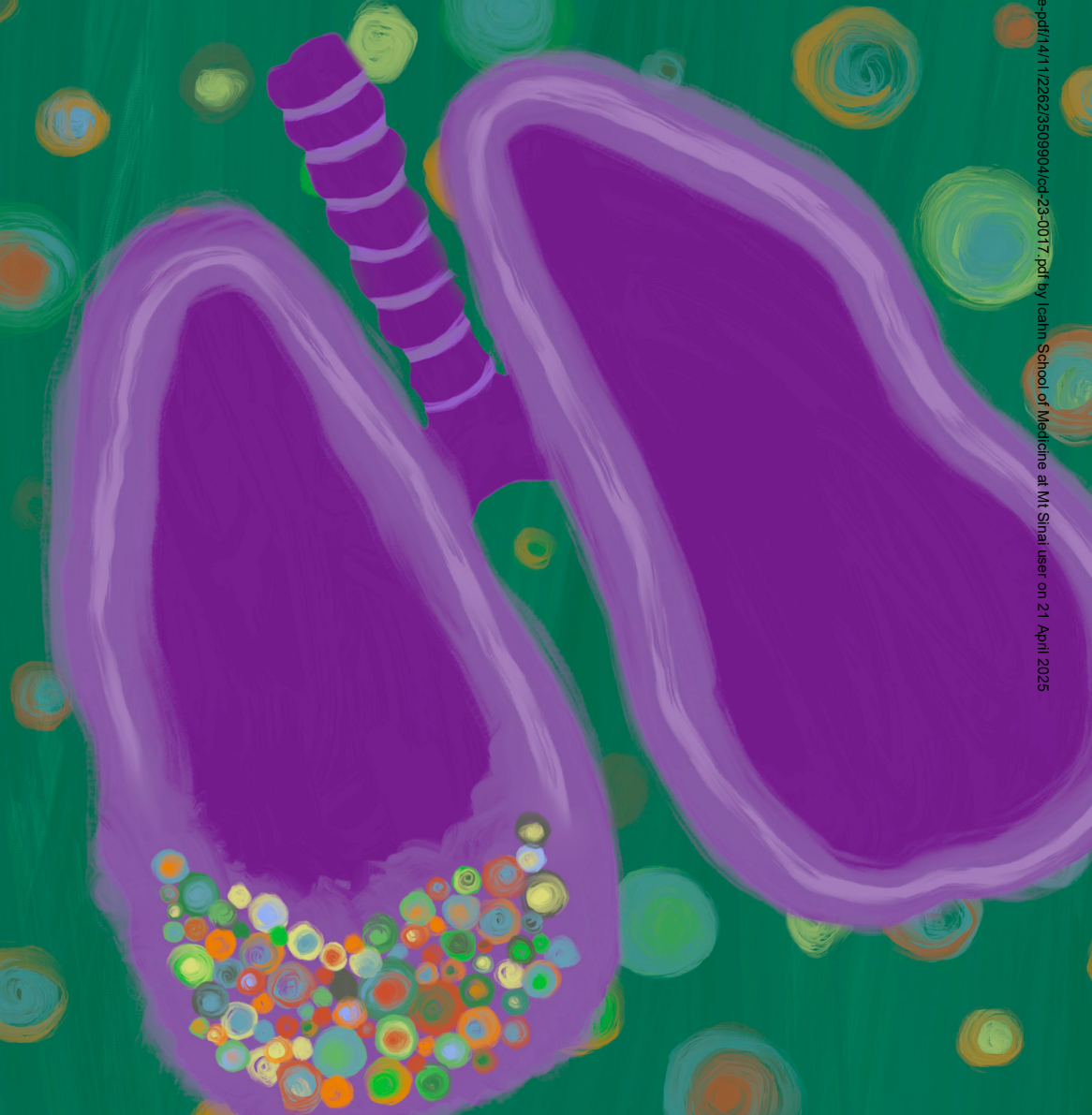


RESEARCH ARTICLE

Single-Cell View of Tumor Microenvironment Gradients in Pleural Mesothelioma



Bruno Giotti^{1,2}, Komal Dolasia^{1,2}, William Zhao^{1,2}, Peiwen Cai^{1,2}, Robert Sweeney^{2,3}, Elliot Merritt^{1,2}, Evgeny Kiner⁴, Grace S. Kim^{1,2}, Atharva Bhagwat^{1,2}, Thinh Nguyen^{1,2}, Samarth Hegde², Bailey G. Fitzgerald⁷, Sanjana Shroff¹, Travis Dawson⁵, Monica Garcia-Barros⁶, Jamshid Abdul-Ghafar⁶, Rachel Chen⁵, Sacha Gnajatic^{2,3}, Alan Soto⁶, Rachel Brody⁶, Seunghee Kim-Schulze⁵, Zhihong Chen⁵, Kristin G. Beaumont¹, Miriam Merad^{2,3}, Raja M. Flores⁸, Robert P. Sebra¹, Amir Horowitz^{2,3}, Thomas U. Marron^{2,3}, Anna Tocheva^{1,2}, Andrea Wolf^{3,8}, and Alexander M. Tsankov^{1,2,3}



ABSTRACT

Immunotherapies have shown great promise in pleural mesothelioma (PM), yet most patients still do not achieve significant clinical response, highlighting the importance of improving the understanding of the tumor microenvironment (TME). Here, we utilized high-throughput, single-cell RNA sequencing (scRNA-seq) to *de novo* identify 54 expression programs and construct a comprehensive cellular catalog of the PM TME. We found four cancer-intrinsic programs associated with poor disease outcome and a novel fetal-like, endothelial cell population that likely responds to VEGF signaling and promotes angiogenesis. Across cellular compartments, we observe substantial difference in the TME associated with a cancer-intrinsic sarcomatoid signature, including enrichment in fetal-like endothelial cells, CXCL9+ macrophages, and cytotoxic, exhausted, and regulatory T cells, which we validated using imaging and bulk deconvolution analyses on independent cohorts. Finally, we show, both computationally and experimentally, that NKG2A:HLA-E interaction between NK and tumor cells represents an important new therapeutic axis in PM, especially for epithelioid cases.

SIGNIFICANCE: This manuscript presents the first single-cell RNA sequencing atlas of PM tumor microenvironment. Findings of translational relevance, validated experimentally and using independent bulk cohorts, include identification of gene programs predictive of survival, a fetal-like endothelial cell population, and NKG2A blockade as a promising new immunotherapeutic intervention in PM.

INTRODUCTION

Pleural mesothelioma (PM) is a cancer of the lung pleura that is strongly associated with exposure to asbestos (1), although the proportion of patients without known occupational asbestos exposure is rising (2). Histologic subtypes can be characterized as epithelioid (60%–75% of cases), sarcomatoid (10%), or biphasic PM (20%–30%), with the latter thought to represent a mixture of epithelioid and sarcomatoid subtypes (3). Due to the aggressive nature of all histologic types, existing therapeutic strategies have had limited success with a median overall survival of approximately 18 months (4, 5). Recently, the combination of anti-PD1 and anti-CTLA4 checkpoint inhibitors has emerged as an effective combination therapeutic option for PM; despite similar response rates

compared with chemotherapy, responses are more durable in this immunotherapy combination, resulting in a 27% decrease in the risk of death (6). Patients with sarcomatoid and biphasic (non-epithelioid) histologies have been historically associated with worst overall survival but are also marked by a higher lymphocyte infiltration (7) in the tumor microenvironment (TME) and show greater benefit from checkpoint blockade combination treatments relative to chemotherapy, which, in contrast, has greater efficacy in epithelioid tumors (6).

Although immunotherapy holds great promise, most patients with PM still do not achieve significant clinical benefit from these therapies, and many who do respond initially only receive a transient benefit. Given the variability in response encountered among patients and the toxicities associated with these therapies, new approaches are needed to determine which patients will benefit from existing immunotherapies and to discover new therapeutic strategies for nonresponders. It is likely that intra- and inter-tumoral heterogeneity in the TME and tumor-immune cell interactions all contribute to the variability in treatment response. Thus, a more complete characterization of the PM TME at baseline will reveal more optimal patient stratification strategies and new immuno-modulatory pathways to target.

Large-scale bulk genomic and transcriptomic studies (8–11) have defined molecular subtypes associated with differences in the TME composition, including higher levels of T cells and M2-like macrophages in sarcomatoid and enhanced VISTA expression in epithelioid PM (8, 9). A subsequent meta-analysis study further reported on higher lymphocyte and monocyte infiltration, and increased stromal components and expression of immune checkpoint (IC) molecules in PM samples correlated with a sarcomatoid transcriptional phenotype (S score), whereas VISTA and NK cell markers trended in the opposite direction (12). Additional studies expanded on the PM tumor-subtype dichotomy to define novel subtypes

¹Department of Genetics and Genomic Sciences, Icahn School of Medicine at Mount Sinai, New York, New York. ²Lipschultz Precision Immunology Institute, Icahn School of Medicine at Mount Sinai, New York, New York. ³Tisch Cancer Institute, Icahn School of Medicine at Mount Sinai, New York, New York. ⁴Immunai, New York, New York. ⁵The Human Immune Monitoring Center, Icahn School of Medicine at Mount Sinai, New York, New York. ⁶Department of Pathology, Molecular and Cell-Based Medicine, Icahn School of Medicine at Mount Sinai, New York, New York. ⁷Department of Hematology and Medical Oncology, Icahn School of Medicine at Mount Sinai, New York, New York. ⁸Department of Thoracic Surgery, Icahn School of Medicine at Mount Sinai, New York, New York.

B. Giotti, K. Dolasia, W. Zhao, and P. Cai contributed equally to this article.

Current address for B.G. Fitzgerald: Roswell Park Comprehensive Cancer Center, Buffalo, New York.

Corresponding Author: Alexander M. Tsankov, Genetics and Genomic Sciences, Icahn School of Medicine at Mount Sinai, One Gustave Levy Place, Box 1498, New York, NY 10029. E-mail: alexander.tsankov@mssm.edu

Cancer Discov 2024;14:2262–78

doi: 10.1158/2159-8290.CD-23-0017

©2024 American Association for Cancer Research

based on additional molecular features such as immune content, DNA methylation, and tumor ploidy (10, 11). Similarly, a recent mass cytometry study based on a 35-antibody panel also identified two histology-independent immunologic subtypes related to MHC-I and MHC-II neopeptide abundance (13). Single-cell RNA sequencing (scRNA-seq) now enables interrogation of the TME at unprecedented resolution and scale without *a priori* knowledge and reliance on a limited set of markers, which has greatly enhanced our understanding of tumor heterogeneity across cancers (14). Here, we used high-throughput scRNA-seq and single-cell T-cell receptor sequencing (scTCR-seq) on treatment-naïve patient samples to build a comprehensive single-cell atlas of PM primary tumor and peripheral blood. Our integrative analysis allowed us to ask if there are cellular and molecular differences in the TME between PM histologic and molecular subtypes, if different subtypes associate with different cancer-intrinsic programs, if new cell-type-specific signatures are predictive of disease outcome, and if the scRNA-seq data can suggest more effective, personalized therapies.

RESULTS

A Single-Cell Catalogue of Patient-Matched PM Tumors and Peripheral Blood

Our study group included 13 treatment-naïve patients diagnosed with PM spanning all three histologic subtypes (Supplementary Table S1) and comprised of four non-white and five female patients (31% and 38% of total cohort, respectively), providing greater diversity compared with national incidence demographics (15). Primary tumor samples were obtained either during surgical resections ($n = 7$) or diagnostic biopsies ($n = 6$) and profiled for scRNA-seq using the 10 \times Chromium platform, including scTCR-seq on seven samples (Fig. 1A). In parallel, peripheral blood mononuclear cells (PBMC) were similarly profiled for a subset of patients ($n = 8$). Following stringent quality control, a total of 141,219 cells were recovered (Supplementary Fig. S1A; "Methods"). We constructed an analytic pipeline (Fig. 1B) aimed at uncovering axes of molecular variation across cellular compartments and PM subtypes in our single-cell data (discovery cohort), which we validated experimentally and *in silico* using bulk RNA-seq and patient survival data from Bueno and colleagues (9) and Hmeljak and colleagues (ref. 8; 293 patients in total, hereafter named Bueno and Hmeljak cohorts, respectively). Unsupervised dimensionality reduction, integration, and clustering of the tumor scRNA-seq data [Fig. 1C (left)] allowed for unbiased discovery of both established and previously unreported PM markers (Fig. 1D; Supplementary Table S2) for all major cell types detected in the tumor samples, including tumor cells (*KRT19*), normal mesothelial cells (*HP*), fibroblasts (*COL1A1*), smooth muscle cells (*MYH11*), endothelial cells (*PECAM1*), myeloid cells (*LYZ*), T cells (*CD3D*), NK cells (*GNLY*), B cells (*CD79A*), plasma cells (*IGLC2*), plasmacytoid dendritic cells (pDC, *IRF8*), a small number of alveolar type II cells (AT2; *SFTPC*), and a rare glial population (*PMP2*) recovered in only one of the patients. Similarly, we identified transcription factors (TFs) specifically expressed in each major cell type (Supplementary Fig. S1B), which uncovered TFs with known roles

in the corresponding cells; for example, TEAD1 in malignant cells, WT1 in mesothelium, and SNAI2 in fibroblasts (16–18). As samples were collected with two different procedures (biopsy or surgical resection), we examined the difference in cell proportions, which showed higher fractions of B, T, and NK cells in the resection samples and malignant cells in the biopsies (Supplementary Fig. S1C). To normalize for sample acquisition differences in cell composition, we performed downstream cell subset and expression program enrichment analyses relative to each cellular compartment and validated our main findings throughout the study with bulk deconvolution analysis.

Additionally, we performed cellular indexing of transcriptomes and epitopes (CITE-seq) to construct a patient-matched single-cell atlas of the cellular protein and 5' transcriptomes of PM PBMCs [Fig. 1C (right)]. Thirty PBMC subsets shared across the eight patients were annotated using a reference-based pipeline ("Methods"), and *de novo* protein and RNA marker discovery identified canonical genes associated with these PBMC annotations, highlighting the quality of the data generated (Supplementary Fig. S1D–S1G; Supplementary Tables S3 and S4).

We next investigated cell-type abundance differences across PM molecular and histologic subtypes using a Bayesian deconvolution framework powered by our PM-specific single-cell expression data ("Methods"). To robustly assess these data, we leveraged both the Bueno and Hmeljak cohorts. Results broadly agreed with previous bulk deconvolution cell-type estimations (11, 12), showing a more prominent infiltrate of T and B lymphocytes and myeloid immune populations as well as a more abundant stromal component in non-epithelioid subtypes, whereas epithelioid tumors were comparatively enriched in malignant and NK cells (Fig. 1E; Supplementary Fig. S1H and S1I; refs. 10–12).

Inference of copy number alterations (CNA) enabled us to distinguish malignant cells from normal mesothelial cells in the tumor scRNA-seq data (Fig. 1F). We detected no malignant cells in biopsy sample P10 and therefore excluded it from all downstream analyses involving cancer cells. The CNA analysis detected large-scale deletions on chromosomes 3 (p-arm), 13, 14, and 22 in most samples, in agreement with frequently deleted regions in PM detected by DNA sequencing (8, 19), which harbor PM commonly deleted genes such as *BAP1*, *LATS2*, and *NF2* (Fig. 1F). Taken together, we have constructed the first comprehensive single-cell catalog of PM and observe clear differences in TME cell compositions between PM subtypes.

De Novo Discovery of PM Cancer Programs Show Link to Disease Outcome

We reasoned that analysis of scRNA-seq data from 30,318 PM malignant cells can provide new, high-resolution insight on intra- and inter-tumoral heterogeneity. Toward this goal, we scored each malignant cell using gene signatures derived from four previously identified PM molecular subtypes (9): sarcomatoid, biphasic-S, biphasic-E, and epithelioid [Fig. 2A (left)]. As expected, we observed that in most sarcomatoid (e.g., P1, P13) and epithelioid (e.g., P8, P9) tumors, malignant cells predominantly reside in the corresponding subtype quadrants [Fig. 2A (right)]. However, several patients' tumors histologically

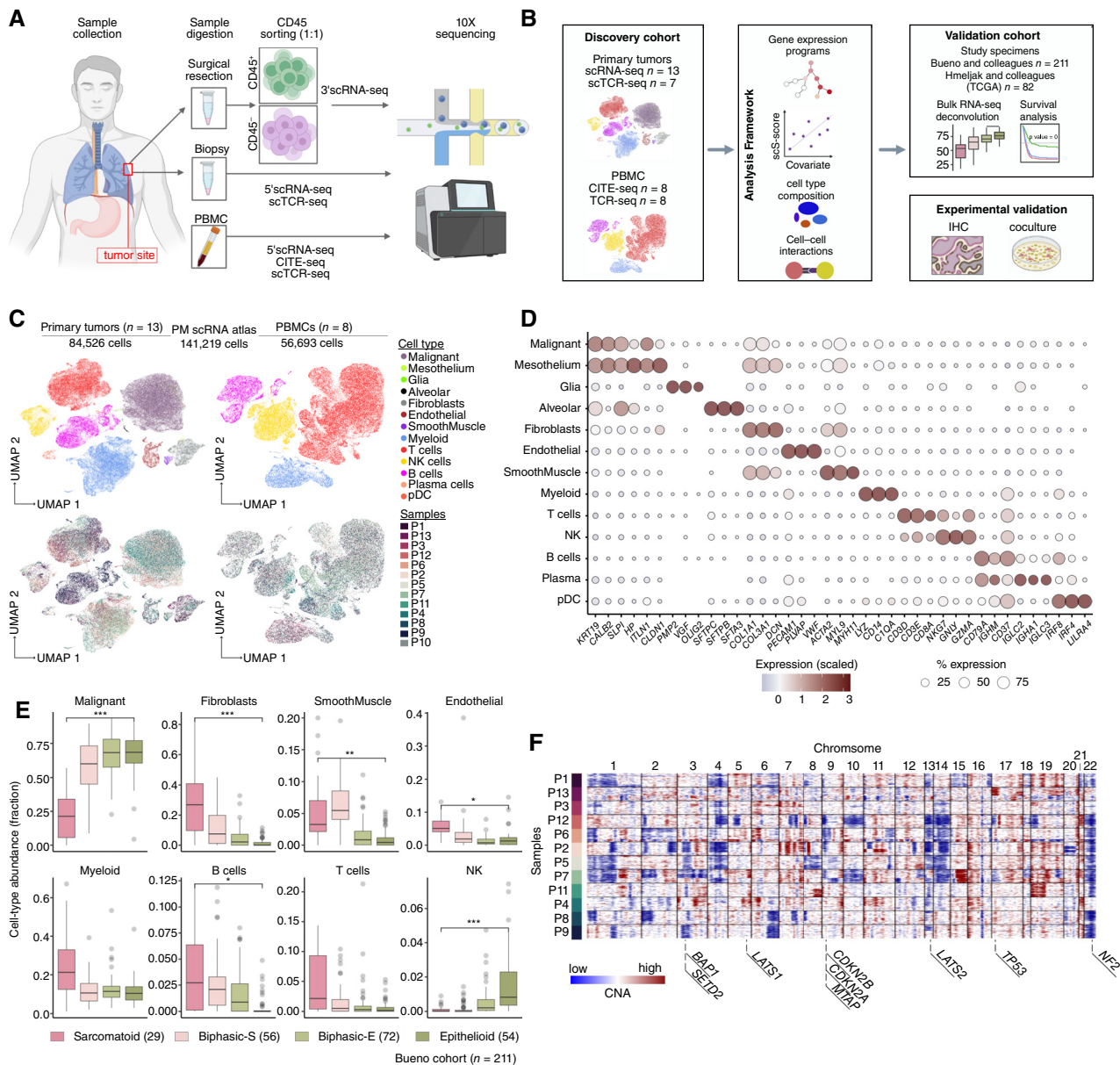


Figure 1. Single-cell catalog of PM tumor and PBMC samples shows distinct TME cell composition differences between molecular subtypes. **A**, Schematic of sample collection, digestion, cell sorting, and sequencing. **B**, Analysis workflow. **C**, UMAP plots colored by cell-type annotations (top) and patient identities (bottom) of primary tumors (left) and PBMCs (right). **D**, Dot plot showing expression and percentage of cells expressing selected marker genes for each annotated cell type. **E**, Sample distributions based on cell-type proportions (deconvolved using BayesPrism) in the Bueno cohort, grouped by different molecular subtypes. FDR-adjusted P values comparing difference between sarcomatoid and epithelioid subtypes were determined by Dirichlet-multinomial regression model that takes into account dependencies in proportions between cell types: *, $P < 0.05$; **, $P < 0.01$; ***, $P < 0.001$. **F**, Inferred CNAs of malignant cells from primary tumor samples (subsampled to 200 cells per patient) with genomic location of key PM driver mutation genes shown on the bottom (A, Created with BioRender.com).

classified as predominantly epithelioid (e.g., P2, P7) were comprised of malignant cells that spanned all four molecular subtypes, uncovering a previously unappreciated intra-tumoral heterogeneity [Fig. 2A (right); Supplementary Fig. S2A]. Taken together, our data supports the view that PM tumors lie on a continuous spectrum between sarcomatoid and epithelioid subtypes (11, 12) and further provides evidence that this paradigm is also valid at single-cell resolution.

The ability of our scRNA-seq analysis to separate malignant cells from other TME cell types enabled us to dissect intra-tumoral heterogeneity and cancer-intrinsic expression programs at a much higher resolution and accuracy than was previously possible in bulk studies. We used consensus non-negative matrix factorization (cNMF, “Methods”) to identify 20 unique cancer modules (Cm1–Cm20) after careful annotation of their biological pathways based on co-expression

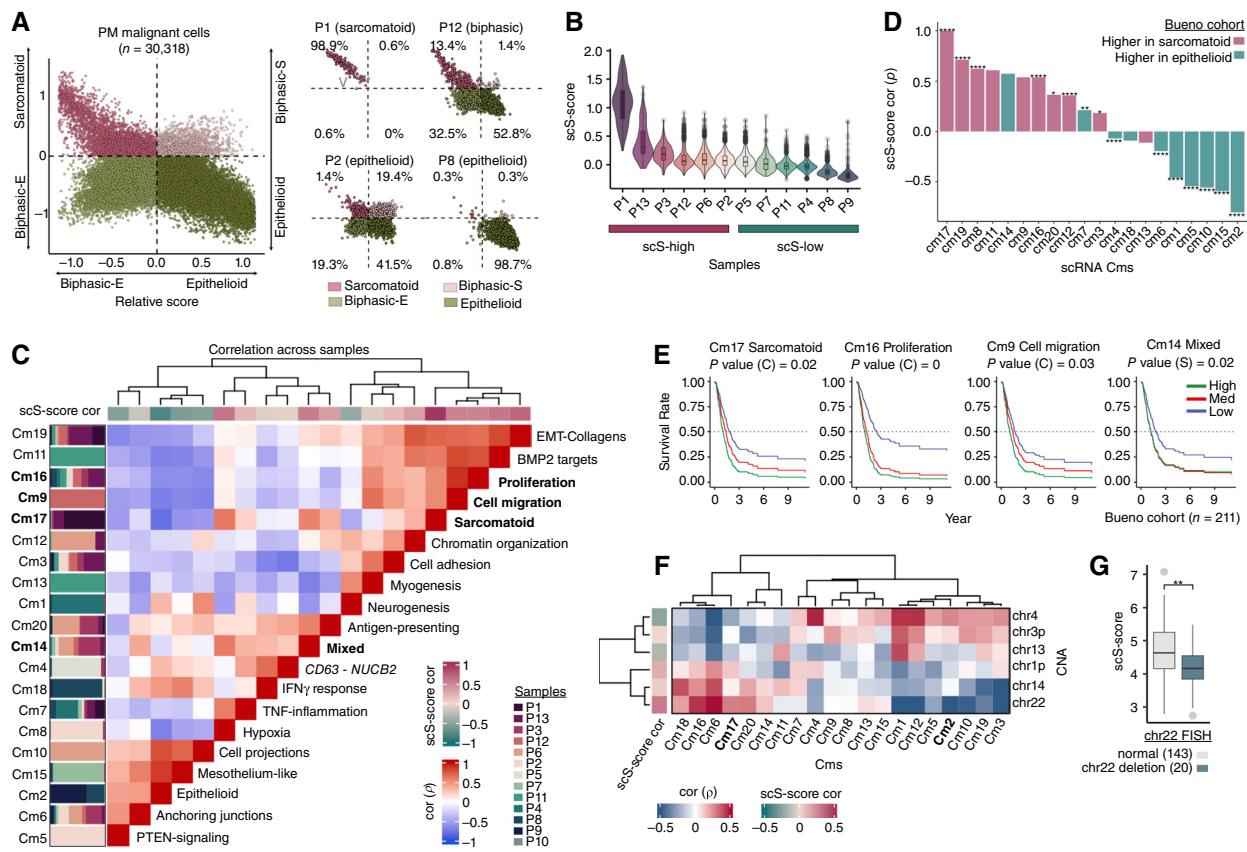


Figure 2. Unbiased discovery of PM cancer programs and association with patient survival. **A**, Left, two-dimensional (2D) representation ("Methods") of the malignant cell distribution across the four PM molecular subtypes (quadrants) defined in Bueno and colleagues (9) combining cells from all patients with PM. Right, 2D representation of the malignant cell distribution for four representative patients with PM. Clinical histology of the cancers upon diagnosis are reported in parentheses. **B**, Per sample malignant cell distribution of the scS-score based on top 20 genes in Cm17, identified *de novo* from the scRNA-seq data. Tumor samples were categorized as scS-high or scS-low based on their mean scS-score ranking. **C**, Pairwise Spearman correlation coefficients (ρ) of sample-averaged scores derived from the 20 Cms identified in malignant cells. Each Cm was annotated with the most representative biological pathway. Vertical stacked bar plots (left) show Cm sample distribution. Top color bar shows correlation of each Cm to the scS-score. **D**, Cm ranked by correlation to the scS-score and colored by their enrichment for either epithelioid (green) or sarcomatoid (red) molecular subtypes from the Bueno cohort. FDR-adjusted P values were computed using Welch's two-sample t test. * $P < 0.05$; ** $P < 0.01$; **** $P < 0.0001$. **E**, Univariate Cox proportional hazard regression analysis (corrected for molecular subtype) for each Cm significantly associated with survival from the Bueno cohort. **F**, Common PM CNA (right) interaction with cancer programs (bottom) as computed by the median of per-sample Spearman correlation coefficients between each Cm and CNA score ("Methods"). Left bar shows median of per-sample Spearman correlation coefficients to the scS-score. **G**, Distribution of samples from the Bueno cohort scored by the scS-score and grouped by FISH staining of chr22 reported as deleted or normal in the Bueno cohort. P value was computed using Welch's two-sample t test. ** $P < 0.01$.

patterns across cells and enrichment of top markers in canonical cancer expression programs (Supplementary Fig. S2B–S2D; Supplementary Table S5). For example, we identified a cancer cell module (Cm17) that was predominantly expressed in sarcomatoid histology tumors and was highly correlated with bulk RNA-seq-derived S score (Supplementary Fig. S2E) from ref. 12. Cm17 included known sarcomatoid-associated genes (e.g., VIM) as well as novel ones such as *IGFBP6* and *CAVIN3* that have been implicated in the progression of breast and lung cancer, respectively (20, 21). To quantify the sarcomatoid content for each sample, we scored all malignant cells for Cm17 (referred to as single-cell sarcomatoid score or scS-score hereafter) and classified tumor samples as scS-high or scS-low based on their mean scS-score ranking (Fig. 2B). To investigate the relationship between different cancer modules and scS-score, we correlated Cm scores across malignant samples

and cells (Fig. 2C; Supplementary Fig. S2B). Cancer modules that most correlated with scS-score included hypoxia (Cm8; *TGFBI*, *VEGFA*), BMP2-driven targets (Cm11; *HPGD*, *SYT1*), epithelial-to-mesenchymal transition (EMT; Cm19; *COL1A1*, *MMP2*), cell migration (Cm9; *BARX1*, *PODXL*), cell proliferation (Cm16; *PCNA*, *MKI67*), and a mixed program expressing EMT, glycolysis, and hypoxia markers (Cm14; *TGFB1*, *LOX*; Supplementary Fig. S2C–D). In contrast, malignant programs that anticorrelated with the scS-score were enriched in epithelioid (Cm2; *MSLN*, *ITLN1*), cell projection (Cm10; *TEAD1*, *WWCI*), and mesothelium markers (Cm15; *HP*, *UPK3B*). We also defined other interesting malignant programs related to immune pathways that did not show strong association with scS-score, including TNF-driven inflammation (Cm7; *NFKBIA*, *ATF3*), interferon response (Cm18; *ISG20*, *IFIT1*), and antigen-presenting programs (Cm20; *HLA-DR*, *HLA-DQ*).

Comparing each module's expression in sarcomatoid versus epithelioid samples in bulk cohorts showed mostly consistent trends, validating our approach (Fig. 2D; Supplementary Fig. S2F). Furthermore, this highlights how our discovery scRNA-seq cohort can be leveraged to uncover novel cancer programs and confirm their association with PM subtypes using large bulk cohorts.

To assess if the *de novo*-discovered cancer programs were associated with different disease outcomes, we performed survival analysis using both the Cox proportional hazards regression analysis (adjusted for molecular subtype or histology) and the Kaplan-Meier model within each histology. We found that sarcomatoid Cm17, cell proliferation Cm16, cell migration Cm9, and mixed program Cm14 were predictive of poor outcome in both validation cohorts (Fig. 2E; Supplementary Fig. S2G and S2H). When stratified by molecular subtype, we also found PTEN-signaling Cm5 and chromatin organization Cm12 to be prognostic of lower overall survival only in epithelioid and sarcomatoid Bueno cohort patients, respectively (Supplementary Fig. S2I).

Lastly, we performed a new computational analysis that systematically uncovers genomic interactions between Cms and expression of genes in frequently deleted PM CNA domains (Fig. 2F; "Methods"). For instance, chromosome 22 (chr22) was anticorrelated with expression of several epithelioid Cms (e.g., Cm2) and positively correlated with scS-score. Interestingly, we observe a similar trend in the Bueno cohort transcriptionally (Supplementary Fig. S2J) and at the DNA level, as quantified by FISH (Fig. 2G), suggesting that chr22 deletions may occur preferentially in low scS-score, epithelioid-like PM tumors.

In summary, single-cell dissection of malignant cell heterogeneity uncovered genomic alterations and cancer-intrinsic gene expression programs in PM associated with different molecular subtypes, including a sarcomatoid, cell proliferation, cell migration, and mixed programs associated with poor outcome.

Fetal-Like, scS-Score-Associated Endothelial Cells Likely Contribute to Angiogenesis

The scRNA-seq data also presented the opportunity to characterize the stromal cell subsets and interactions across our cohort, which has been largely understudied in PM compared with the malignant and immune cell compartments. Based on Louvain clustering and expression of canonical markers, we identified six mesenchymal and endothelial cell (EC) subsets: artery, *PLVAP*⁺ EC, vein, lymphatic EC (LEC), cancer-associated fibroblasts (CAF), and smooth muscle cells (Fig. 3A and B; Supplementary Fig. S3A). Using cNMF, we identified six EC gene modules (Ems), where only Em3 *PLVAP*⁺ EC module was positively correlated with the cancer-intrinsic scS-score (Supplementary Fig. S3B and S3C). cNMF also uncovered six CAF modules (Fms): *COL6A2*^{high}*PNISR*^{high} (Fm1), *IGFBP6*^{high}*MFAPS*^{high} (Fm2), *CDH2*^{high}*FABP5*^{high} (Fm3), *COL16A1*^{high}*COL8A1*^{high} (Fm4), *TXNIP*^{high}*SERPING1*^{high} (Fm5), and *IGFBP2*^{high} (Fm6; Supplementary Fig. S3D and S3E). Comparison with mesenchymal cells from normal lung scRNA-seq data (22) revealed that Fm1–2 were correlated with adventitial fibroblasts, Fm4 with alveolar fibroblast, Fm3 with pericytes, and Fm5–6 with lipofibroblast transcriptomes (Supplementary Fig. S3F).

Integration with normal lung EC scRNA-seq data (22) similarly confirmed high correspondence between normal and PM EC subsets, except for the *PLVAP*⁺ EC population (Fig. 3C). To examine the functional role of this EC subset, we performed gene set enrichment analysis and found high enrichment of genes associated with blood vessel morphogenesis and development (Fig. 3D). This suggested that *PLVAP*⁺ ECs may be more prominent in development and prompted us to compare this population to a recently published fetal lung single-cell atlas (23); indeed, top markers expressed in *PLVAP*⁺ ECs were also highly expressed in distal fetal lung endothelial populations (Fig. 3E) relative to EC subset from adult lungs (22). *PLVAP* was recently reported as a marker for fetal-like ECs in hepatocellular carcinoma, but other marker genes (e.g., *COL4A1/2*, *RGCC*, *HSPG2*, *COL15A1*) were unique to this population arguing that this is a PM-specific, fetal-like EC subset (24).

Next, we employed single-cell regulatory network and clustering (SCENIC, "Methods") to decipher the key TF and downstream gene regulatory modules (regulons) for each EC subset (Supplementary Fig. S3G). This analysis revealed ETS1 and MEF2C to be among the top TF regulators of *PLVAP*⁺ EC population, including 318 and 63 genes in their regulons, respectively. Both *de novo*-identified ETS1 and MEF2C regulons were most highly expressed in the *PLVAP*⁺ EC and fetal EC subpopulations (Fig. 3F; Supplementary Table S6). In agreement, ETS1 and MEF2C are known to be required for endothelial patterning in embryonic angiogenesis (25, 26) and are also known to regulate angiogenesis (27).

To examine which TME signaling pathways are most likely to regulate the gene expression of *PLVAP*⁺ ECs, we employed NicheNet ("Methods") and found that VEGFA was the top predicted ligand, expressed predominantly in myeloid and tumor cells (Fig. 3G). Not surprisingly, *PLVAP*⁺ ECs also showed the highest expression of VEGFA receptors KDR and FLT4 (Supplementary Fig. S3H). It is worth noting that in the Hmeljak cohort, the combined expression of highly specific markers for *PLVAP*⁺ EC subset was significantly correlated with poor survival (Supplementary Fig. S3I). Furthermore, *PLVAP*⁺ EC expression was enriched in scS-high, non-epithelioid PM in bulk RNA cohorts after correcting for endothelial content (Fig. 3H; Supplementary Fig. S3J).

To experimentally validate the presence of *PLVAP*⁺ ECs in PM and enrichment in non-epithelioid tumors, we performed dual immunohistochemistry staining for PLVAP and CD31 on tissue sections derived from patients with PM encompassing all three histologic subtypes, along with uninvolving normal distal lung tissue (control) obtained from patients with lung adenocarcinoma. The quantified percentages of endothelial cells exhibiting concurrent expression of CD31 and PLVAP within blood vessels were significantly increased in PM compared with control tissue, with the largest differences observed in non-epithelioid PM (Fig. 3I and J). Taken together, we discovered a PM-specific, fetal-like, angiogenic *PLVAP*⁺ EC subset that is likely regulated by TFs ETS1, MEF2C, and VEGFA signaling; this population specifically expresses VEGFA receptors KDR and FLT4 and is enriched in non-epithelioid PM tumors, which likely favors tumor survival and contributes

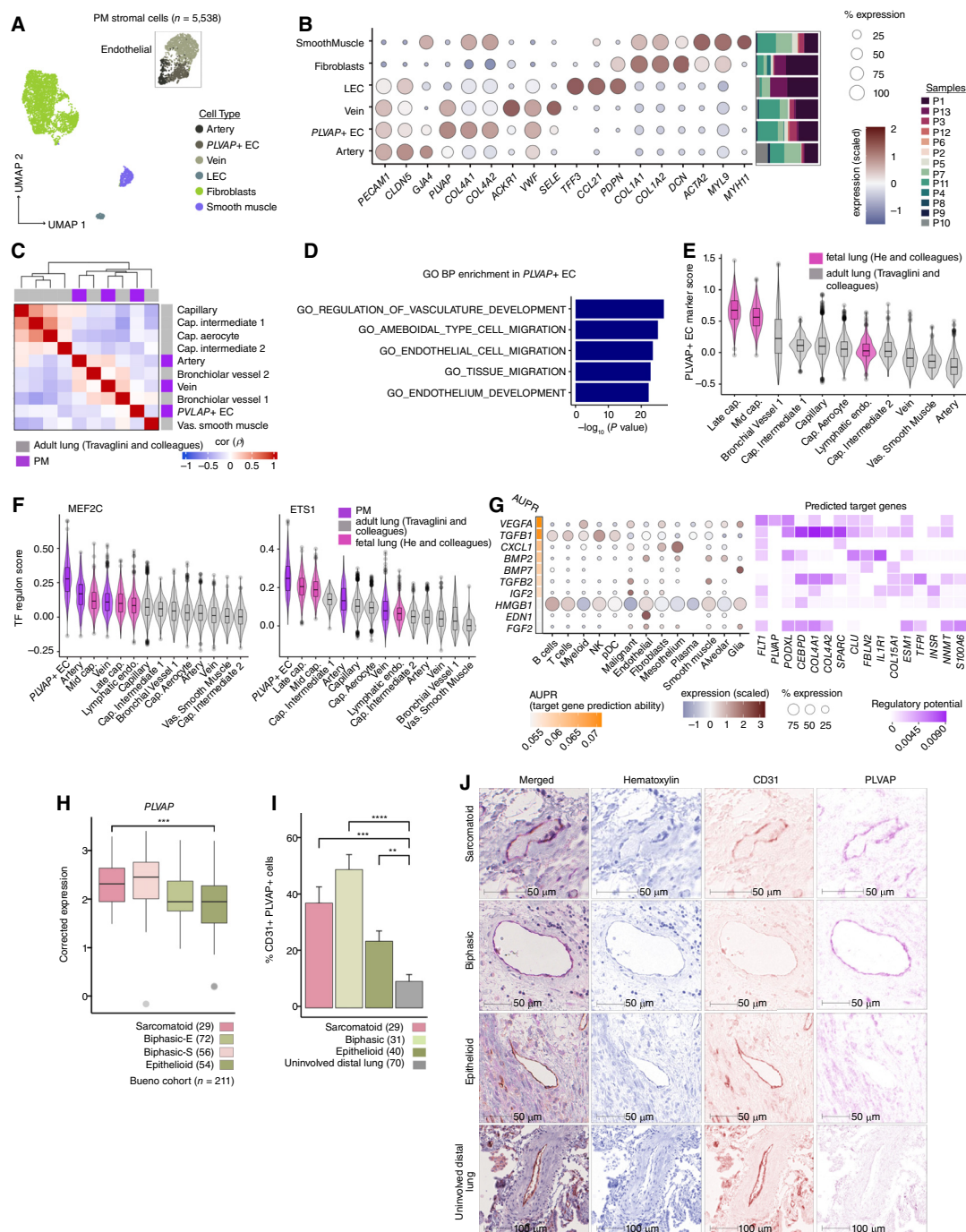


Figure 3. Fetal-like, cancer-enriched PLVAP+ endothelial cells associate with angiogenesis. **A**, UMAP embeddings of PM stromal and endothelial cell types integrated across patients. **B**, Dot plot showing expression and percentage of cells expressing top selected markers per cell-type annotation with relative sample composition for each cell type (right, stacked bar plots). **C**, Spearman correlation coefficients (ρ) heatmap clustering the average expression profiles of endothelial cell subsets found in normal adult distal lung and PM samples. **D**, Gene set enrichment analysis in PLVAP+ EC markers compared against the Gene Ontology biological processes (GO BP) database. Top five enriched categories are displayed. **E**, Distribution of PLVAP+ EC marker score in fetal and adult distal lung endothelial cell subsets, ordered from highest to lowest median score. **F**, Distributions of the MEF2C (left) and ETS1 (right) regulon activity in fetal, adult distal lung, and PM endothelial cell subsets. **G**, NicheNet prediction of ligand prioritization (top 10 displayed), their abundance in sender cell types (left dot plot), and their cognate targets among PLVAP+ EC markers (right heatmap). **H**, Sample distributions of PLVAP expression in the Bueno cohort grouped by molecular subtype after correcting for endothelial content. P values were computed comparing sarcomatoid and epithelioid subtypes using Welch's two-sample t test. *** P < 0.001. **I**, Quantification of IHC staining of PLVAP+ CD31+ endothelial cells in PM tumor tissue sections of sarcomatoid ($n = 2$), biphasic ($n = 2$), and epithelioid histology ($n = 2$) compared with normal adjacent distal lungs ($n = 4$). Between 9 and 23 ROI were quantified for each sample. P values were computed comparing each PM subtype to the normal tissue using Welch's two-sample t test. ** P < 0.01; *** P < 0.001; **** P < 0.0001. **J**, Representative micrographs from tissue sections from patients with sarcomatoid, biphasic, and epithelioid PM histologies and uninvolved normal distal lung tissue section stained with anti-PLVAP (purple), CD31 (brown), and hematoxylin (blue). Cap., capillary; Vas., vascular; Endo., endothelial.

to a worse disease outcome. These findings thus support further investigation of anti-VEGFA agents (5) in PM tumors with high *PLVAP*⁺ EC abundance.

Macrophages in scS-High PM Express CXCL9/10/11 and Likely Contribute to T-cell Infiltration

To characterize the diversity of myeloid cells in PM, we performed unsupervised clustering followed by integration and annotation of cell subtypes based on canonical markers. We identified eight different myeloid subsets: dendritic cells, further separated into cDC1, cDC2, and mregDCs, plasmacytoid dendritic cells (pDC), classical (CD14⁺) and nonclassical (CD16⁺) monocytes, mast cells, and a large and heterogeneous cluster of tumor-associated macrophages (TAMs; Fig. 4A and B; Supplementary Fig. S4A–S4C). We observed that *VISTA*, an IC gene shown to be preferentially expressed in epithelioid subtypes (8, 28), was most highly expressed by monocytes among myeloid subsets and all other cell types and showed elevated expression in scS-low vs scS-high tumor monocytes (Fig. 4C). *VISTA* has been targeted in clinical trials for PM, and quantifying its expression at a single-cell resolution can elucidate the cellular context of its potential therapeutic mechanisms and how these differ across histologic subtypes.

When applying cNMF to dissect TAM heterogeneity, we detected 10 macrophage modules (Mms), including an interstitial macrophage-like state (Mm1; *SELENOP*, *LYVE1*), an inflammatory *CXCL9*^{high} TAM state (Mm6; *C1QC*, *STAT1*), and lipid-associated *TREM2*^{high} TAM state (Mm7 and Mm9; *SPP1*, *TREM2*; Fig. 4D; Supplementary Fig. S4D and S4E). We find that Mm1 and Mm6 were most correlated with the scS-score (Fig. 4D). In agreement, *CXCL9/10/11* expression was higher in scS-high versus scS-low myeloid cells (Fig. 4E and F). These chemokines are known to bind receptor CXCR3, recruit T cells to the tumor core, and correlate in expression with lymphocyte abundance in melanoma and lung cancer (29, 30). In our cohort, *CXCL9/10/11* were most highly expressed in monocytes and TAMs, whereas their corresponding receptor CXCR3 was specifically expressed in NK and T cells, especially in CD8 and regulatory T (Treg) cells (Fig. 4F). Increased recruitment of T cells in scS-high PM tumors via these interactions is further supported by significant correlations between *CXCL9/10/11* expression and T-cell abundance in the Bueno cohort (Fig. 4G).

To further investigate the regulation underlying different myeloid and TAM subsets, we performed regulon analysis using SCENIC (Fig. 4H; Supplementary Fig. S4F). This *de novo* analysis captures the known role of *IRF8* in cDC1 survival and pDC function (Supplementary Fig. S4F; ref. 31). Additionally, TFs *MAF*, *ATF3*, and *JUN* were enriched for regulon activity with scS-high associated Mm1 TAM state, whereas known IFN γ signaling TFs *STAT1* and *IRF1* (32) were predicted as regulators of Mm6 and *CXCL9/10/11* expression (Fig. 4H).

In summary, we observe differences in myeloid expression associated with different PM subtypes—scS-low tumors exhibit higher *VISTA* expression in monocytes and scS-high tumors show increased TAM production of *CXCL9/10/11* chemokines, which are implicated in chemotaxis of T cells and likely regulated by TFs *STAT1* and *IRF1*. These findings can inform on future immunomodulatory therapies targeting myeloid cells in PM.

Molecular Dissection of T-cell Programs and IC Molecules Show Association with scS-Score

To comprehensively characterize the T and NK cellular diversity in PM *de novo*, we again utilized two complementary unsupervised clustering approaches: Louvain clustering and cNMF. Louvain clustering identified major cell subsets in the tumor samples including CD4, CD8, NK-like T cells, Treg, T follicular helper (T_{FH}) cells, and two NK cell subsets marked by high expression of *KLRC1* and *FGFBP2* (Fig. 5A and B; Supplementary Fig. S5A). Using cNMF, we additionally uncovered functional T-cell expression modules (Tm), such as naïve (Tm1), stress response (Tm8), interferon response (Tm12), inflammatory (Tm3), and gamma delta modules (Tm9; Fig. 5C; Supplementary Fig. S5B and S5C). We found six T-cell modules highly correlated with scS-score (Fig. 5C and D), including proliferative (Tm10) and Treg programs (Tm7; *FOXP3* and *IL2RA*), and four other modules linked to CD8 cell states: progenitor (Tm11; *XCL1*, *GNG4*), exhaustion (Tm5; *HAVCR2*, *LAG3*), effector (Tm2; *NKG7*, *GZMA*), and MHC II genes expressing module (Tm4) linked to CD8 T-cell activation (33). CD8 T-cell effector, exhaustion, and Treg modules showed increased expression in T cells from scS-high tumors and were significantly enriched in bulk deconvolution analysis comparing sarcomatoid versus epithelioid tumors after correcting for T-cell content ("Methods"), arguing that higher immune infiltration in scS-high tumors is accompanied by a shift toward CD8 and Treg fractions (Fig. 5E; Supplementary Fig. S5D). Increased exhaustion in scS-high T cells was also supported by higher expression of *HAVCR2* and *LAG3* as well as known IC targets *PDCD1*, *TIGIT*, and *CTLA4* (Fig. 5F), as previously reported in bulk RNA-seq studies (11, 12). Among T-cell subsets, *CTLA4* and *TIGIT* showed highest expression in Tregs, whereas *PDCD1* was most highly expressed in CD8 and T_{FH} cells in scS-high and scS-low tumors, respectively (Fig. 5G; Supplementary Fig. S5E).

We observed an expression of germinal center (GC) T_{FH} cell (34) markers (e.g., *TOX2*, *CXCR5*) in a sample P9-enriched module Tm6 (Fig. 5H), prompting us to examine the B-cell compartment where we also identified a population of highly proliferative GC B cells found almost exclusively in P9 (Fig. 5I and J). Notably, enrichment of both GC T_{FH} and B cells suggests the presence of mature tertiary lymphoid structures (TLS) in this patient with epithelioid PM. To investigate a link between TLS presence and molecular subtypes, we correlated the expression of GC T_{FH} marker *TOX2* with the top markers of GC B cells (Fig. 5J) and found a significant association only in epithelioid samples (Fig. 5K; $\rho = 0.21$, P value = 0.0004). Interestingly, a previous study showed histologic evidence of TLS presence in a subset of epithelioid PM tumors associated with longer survival (35).

Next, we examined the CITE-seq and scTCR-seq data for all PBMC lymphocytes, which showed consistent RNA and protein expression (Fig. 5L and M; Supplementary Fig. S5F) and detection of more than 3,000 expanded clonotypes in CD8 T cells (Supplementary Fig. S5G). Expanded TCR clonotypes may be indicative of reactive CD8 T cells recognizing tumor antigens or bystander CD8 memory T cells, but only the former may lead to terminal exhaustion (36). Hence, we scored CD8 T cells with detectable TCR sequence by the exhaustion module previously

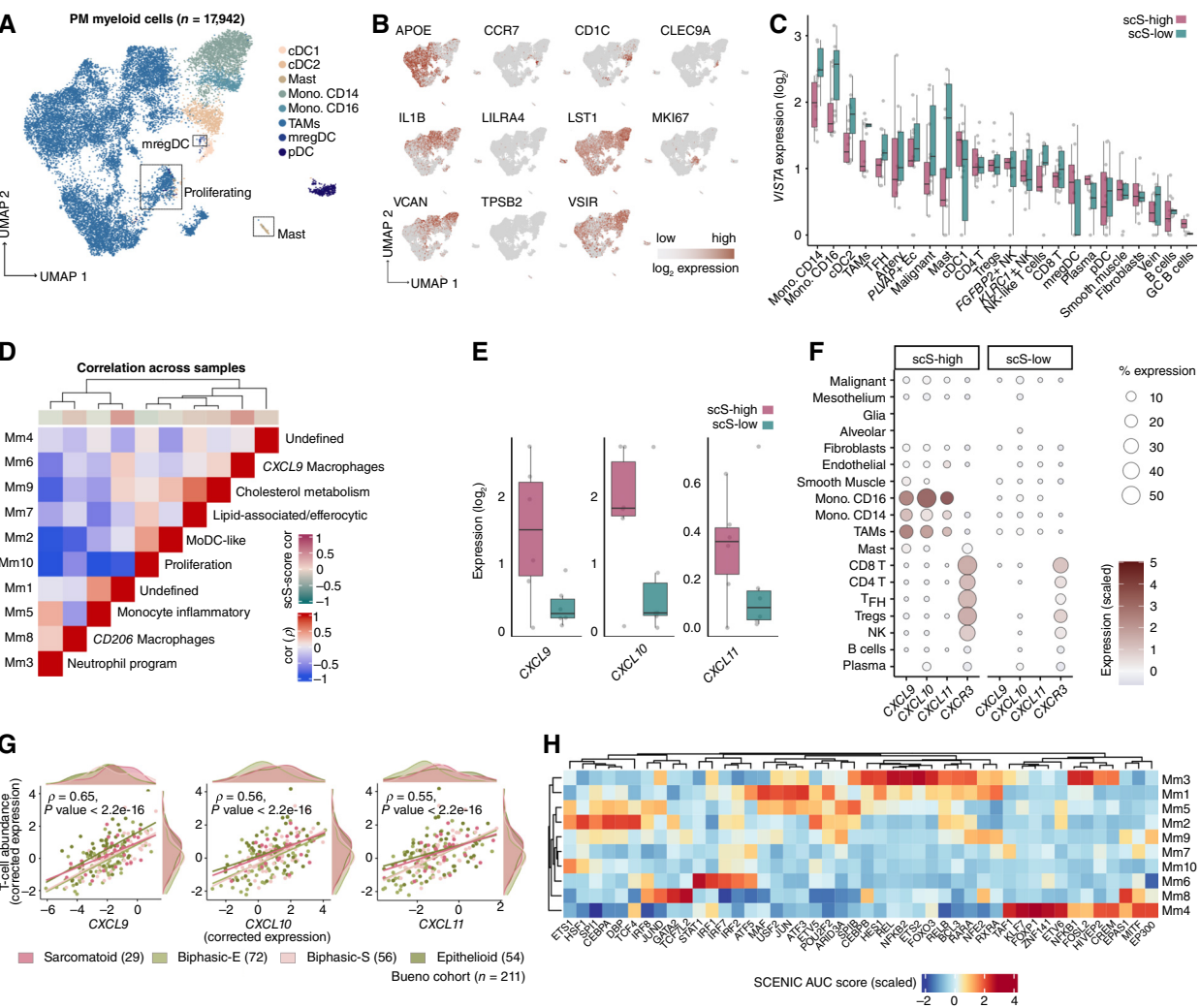


Figure 4. Macrophages in scS-high PM express CXCL9/10/11 and likely contribute to T-cell infiltration. **A**, UMAP embeddings of PM myeloid cells integrated across patients. **B**, Feature plots of key markers used for myeloid cell-type annotation. **C**, Sample distributions of \log_2 -normalized expression levels of VSIR (VISTA) across all PM cell types, including myeloid subsets and split by scS-high and scS-low samples. FDR-adjusted P values were computed using Welch's two-sample t test. **D**, Pairwise Spearman correlation coefficients (ρ) of sample-averaged scores derived from the 10 Mms identified in PM TAM. Each Mm was annotated with the most representative biological pathway. Top color bar shows correlation of each Mm to the scS-score. **E**, Sample distributions of \log_2 -normalized mean TAM expression of CXCL9/10/11 split by scS-high and scS-low samples. FDR-adjusted P values were computed using Welch's two-sample t test. **F**, Dot plot showing expression and percentage of cells expressing CXCL9/10/11 and their receptor CXCR3 across cell types and split by scS-high and scS-low samples. **G**, Expression of CXCL9/10/11 vs. T-cell abundance inferred as the average expression of T-cell marker genes in the Bueno cohort corrected for immune content. Spearman correlation P values are shown. **H**, Heatmap of the SCENIC significant regulon activities (scaled AUC score) and correspondent TFs (columns) in each Mm. TAM, tumor-associated macrophage; T_{FH} , T follicular helper cell; Treg, regulatory T cell.

identified in tumor-infiltrating lymphocytes (Tm5) and found that expanded CD8 clonotypes have significantly higher exhaustion score compared with non-expanded clonotypes (Fig. 5N). We also show significant increases for activation (Tm4) and cytotoxicity (Tm2) of CD8 module scores (Supplementary Fig. S5H). These trends were also observed in tumor-infiltrated T cells, albeit not significant perhaps due to smaller sample size, where expanded clonotypes were also mapped primarily to CD8 T cells and made up a higher fraction of CD8 T cells in scS-high tumors (Supplementary Fig. S5I–S5K). Finally, we identified several expanded clonotypes present in both tumor and blood patient-matched samples that exhibit high exhaustion scores, further suggesting systemic antitumoral T-cell activity (Fig. 5O; Supplementary Fig. S5L and S5M).

Taken together, molecular characterization of B and T cells revealed a higher Treg abundance, IC target expression, and CD8 exhaustion, cytotoxicity, and activation modules associated with the scS-score; in contrast, germinal center T_{FH} and B-cell markers suggest preferential TLS formation in epithelioid PM tumors.

NK Cell IC Blockade Targeting NKG2A as a Novel Therapeutic Strategy in PM

In the past decade, immunomodulatory drugs have become a mainstay for the treatment of cancer, including anti-PD1 and anti-CTLA4 combination therapy recently approved for use in PM (6). NK cells have been largely unexplored in PM but also represent a viable therapeutic target (37). We found a

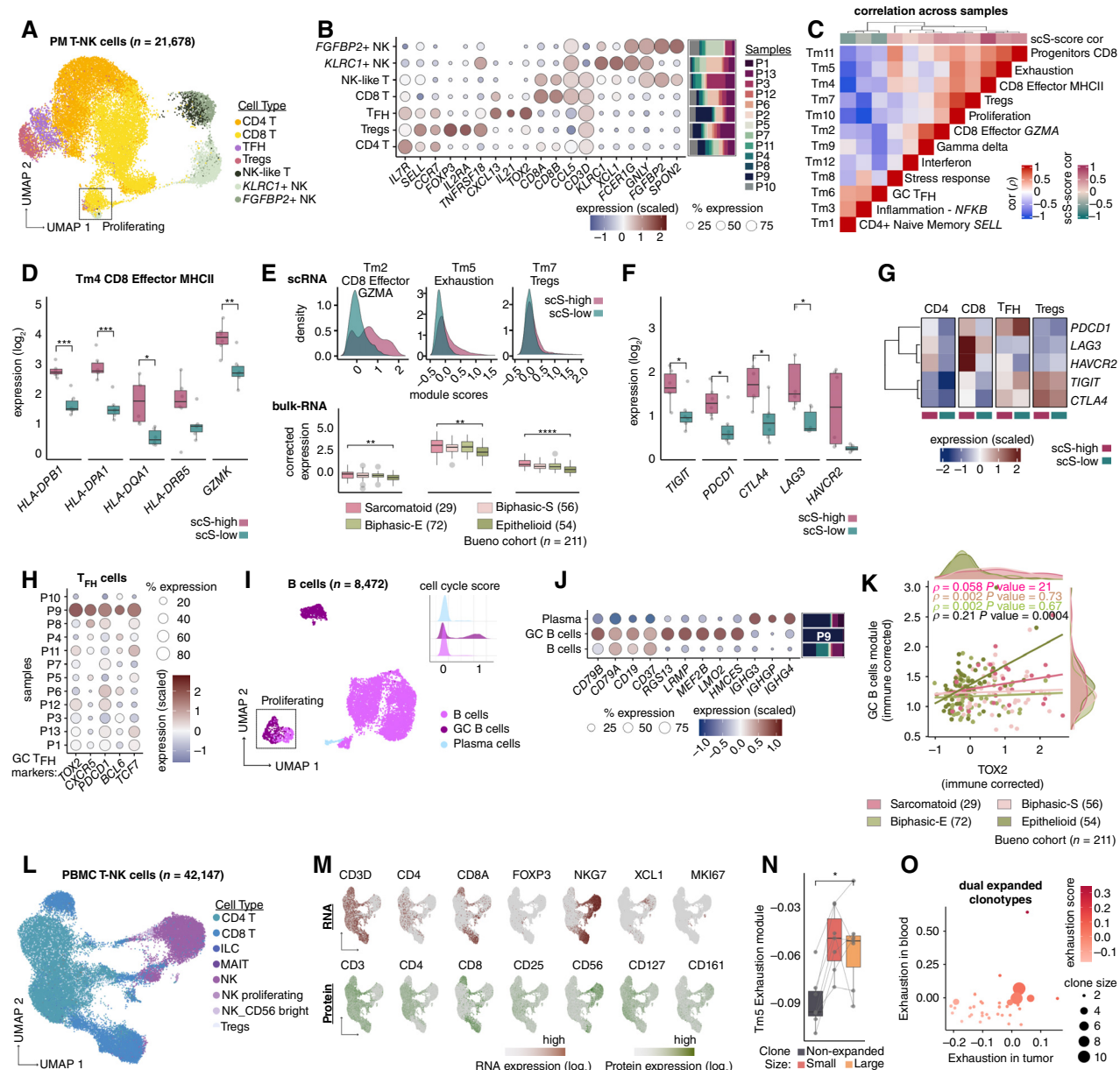


Figure 5. Molecular dissection of T-cell programs and IC molecules shows association with scS-score. **A**, UMAP embeddings of PM tumor T and NK cells integrated across patients. **B**, Dot plot showing the expression and percentage of cells expressing key markers used for cell-type annotation with relative sample composition for each cell type (right, stacked bar plots). **C**, Pairwise Spearman correlation coefficients (ρ) of sample-averaged scores derived from the 10 Tms identified in T cells. Each Tm was annotated with the most representative biological pathway. Top color bar shows correlation of each Tm to the scS-score. **D**, Sample distributions of log₂-normalized mean T-cell expression of selected genes from Tm4 averaged per samples and split by scS-high and scS-low samples. FDR-adjusted *P* values were computed using Welch's two-sample *t* test. *, *P* < 0.05; **, *P* < 0.01; ***, *P* < 0.001. **E**, Cell distributions of Tm module scores in all scS-high and scS-low samples (top) and sample distributions of Tm expression in the Bueno cohort for each PM molecular subtype after correcting for immune content (bottom). FDR-adjusted *P* values were computed comparing sarcomatoid and epithelioid subtypes using Welch's two-sample *t* test. **F**, Sample distributions of log₂-normalized mean T-cell expression of known IC molecules. FDR-adjusted *P* values were computed using Welch's two-sample *t* test. *, *P* < 0.05. **G**, Scaled log₂-normalized mean expression of known IC molecules across T-cell subsets in scS-high and scS-low samples. **H**, Dot plot showing the expression and percentage of cells expressing markers for germinal center TFH cells identified in Tm6. **I**, UMAP of B-cell compartment, including germinal center B cells (GC-B cell) predominantly found in P9. Inset shows distribution of cell cycle scores grouped by B-cell subsets. **J**, Dot plot showing the expression and percentage of cells expressing top markers of B-cell subsets and relative sample composition (right, stacked bar plots). **K**, Average expression of marker genes of GC B cells (y axis) vs. expression of TOX2 (identifying GC T_{FH} cells, x axis) in the Bueno cohort corrected for immune content. Spearman correlation coefficients and relative *P* values were computed for each molecular subtype. **L**, UMAP embedding of annotated T and NK cell subsets integrated across all PBMC samples. **M**, Feature plots of T and NK cell subset representative markers (top, RNA; bottom, protein). **N**, Sample distribution of the mean Tm5 exhaustion score in non-expanded vs. expanded (split into small and large groups) clonotype CD8 cells from PBMC samples. *P* value was computed using Welch's two-sample *t* test. *, *P* < 0.05. **O**, Dual expanded clonotypes as identified both in patient-matched tumor and PBMC samples distributed by their exhaustion scores in the corresponding sample source.

significant survival benefit of higher NK cell infiltration in tumors from patients with epithelioid PM (Fig. 6A; Supplementary Fig. S6A) and observe a similar trend when using a Cox proportional hazard regression model across all subtypes in both validation cohorts (Supplementary Fig. S6B and S6C). Combined with our previous observation of higher NK cell infiltration in epithelioid PM (Fig. 1E), this analysis indicates that NK cell abundance may represent an important, epithelioid-specific prognostic biomarker. To dissect the crosstalk between NK and malignant cells and identify new therapeutic avenues, we curated a list of NK cell inhibitory receptors and cognate ligands and found that *KLRC1* and its ligand *HLA-E* were both highly expressed by NK and malignant cells, respectively, in comparison to other ligand receptor pairs in our scRNA-seq data (Fig. 6B). *KLRC1*-expressing NK cells were also most abundant in PM compared with other cancer types (Fig. 6C) after integrating our scRNA-seq data with a pan-cancer immune cell atlas (38), and median expression of *KLRC1* and *HLA-E* in PM was the fifth highest among 33 cancer types surveyed in The Cancer Genome Atlas (TCGA; Supplementary Fig. S6D).

Antibodies (e.g. monalizumab) targeting NKG2A (encoded by *KLRC1* gene) have been shown to enhance both NK and CD8 T-cell response (37). To experimentally test if blocking NKG2A/*HLA-E* interaction could augment NK cell antitumor function in PM, we cocultured four mesothelioma cell lines with blood-derived NK cells in the presence or absence of anti-NKG2A antibody (Fig. 6D; Supplementary Fig. S6E). Flow cytometry analysis showed that the mesothelioma cell lines constitutively express HLA-E, which increased following IFN γ treatment (Supplementary Fig. S6F), whereas the NK cells expressed high levels of NKG2A (Supplementary Fig. S6G). Next, NK cells were cocultured with the mesothelioma cell lines for 16 hours in the presence or absence of anti-NKG2A antibody, and, as readouts for NK cell activation, IFN γ production and degranulation (CD107a $^+$, granzyme A $^{-low}$) were measured thereafter by flow cytometry. We found that NKG2A blockade significantly increased NK degranulation and IFN γ production, regardless of whether the tumor cell lines were pre-stimulated with IFN γ to increase HLA-E expression (Fig. 6E). These differences remained significant after applying a Boolean operator for gating on total activated NK cells undergoing degranulation or producing IFN γ (Supplementary Fig. S6H). We tested this interaction also in the presence of anti-MHC class I (MHCI) antibody because the expression of MHCI on tumor cells is known to suppress NK cell activation. This additional step confirmed that enhanced NK cell activation was indeed primarily due to the targeted blockade of the NKG2A:HLA-E interaction (Fig. 6E; Supplementary Fig. S6H).

In conclusion, our analysis demonstrates that NK cell infiltration is a prognostically relevant biomarker in epithelioid PM subtypes and that targeting NKG2A significantly augments NK cell tumor cytotoxicity, warranting further investigations as a viable immunotherapy strategy in PM.

DISCUSSION

We performed scRNA-seq profiling of ~140,000 human tumor and peripheral blood cells and identified 54 gene expression modules across cellular compartments to generate

the first single-cell sequencing atlas of PM. Analysis of malignant cell heterogeneity showed the presence of all four molecular subtypes in biphasic and most epithelioid PM tumors, supporting the notion that PM tumors do not classify into discrete molecular subtypes but rather lie on a continuum between sarcomatoid and epithelioid histology (11, 12). Consequently, we adopted a rank-based analytical strategy designed to capture enrichments of different cellular programs across patients that uncovered a highly distinct TME associated with a cancer-intrinsic sarcomatoid signature, which we termed scS-score (Fig. 6F). We also uncovered new cell migration, proliferation, and mixed hypoxia/EMT cancer modules that were associated with high scS-score across patients and predictive of poor outcome. In contrast, cancer modules containing epithelioid markers were associated with chromosome 22 deletion in our scRNA-seq data, which was supported by RNA expression and DNA FISH data from the Bueno cohort.

Our *de novo* analysis led to the discovery of a fetal-like, *PLVAP* $^+$ EC population, which we predict responds to VEGFA signaling via receptors KDR and FLT4 and promotes angiogenesis. This population was enriched in PM tumors when compared with ECs from adult lungs and was also associated high scS-score (scS-high) samples, which we validated by IHC. Bevacizumab, a monoclonal antibody targeting VEGFA, effective in the treatment of many cancers (39), has been introduced in first-line standard of care for patients with unresectable PM albeit with limited benefits (5). Efforts in identifying biomarkers of treatment response have focused on plasma levels of VEGFA and molecules eliciting similar angiogenic responses with inconclusive results (40, 41). It is tempting to speculate that this population of *PLVAP* $^+$ ECs may represent a novel biomarker for antiangiogenic therapy response and a putative future drug target to abrogate tumor-induced angiogenesis.

Examination of the immune composition of PM samples with high scS-score showed a higher proportion of Tregs and CD8 effector and exhausted T cells, in line with past bulk RNA studies (10, 11), and further uncovered a population of CD8 MHCII $^+$ T cells, which was previously reported to induce pro-inflammatory activity in patients responding to neoadjuvant chemotherapy in breast cancer (33). We also provide molecular evidence for T_{FH} cells positive for CXCL13 and IL21, which are relevant biomarkers of immunotherapy response (42), and further describe a patient-specific TOX2 $^+$ T_{FH} transcriptional program associated with the presence of highly proliferating germinal center B cells that could signify the presence of mature TLSs (43). Indeed, *Tox2* has been shown to be essential for maintaining a T_{FH} phenotype when transfected in GC T_{FH} isolated from human tonsils *ex vivo* (34). Supporting our finding, TLSs have been previously observed in PM using bulk RNA and histologic analysis on a cohort of 123 chemo-naïve patients, which was linked to improved survival and enriched in epithelioid tumors (35). Finally, we identified a CXCL9/10/11-expressing TAM population in PM that is associated with high scS-score samples and likely contributes to chemotaxis for T-cell trafficking to the tumor core. Consistent with this observation, CXCR3 (receptor for CXCL9/10/11) was more expressed in scS-high tumor T cells, especially in CD8 T cells and Tregs that have higher

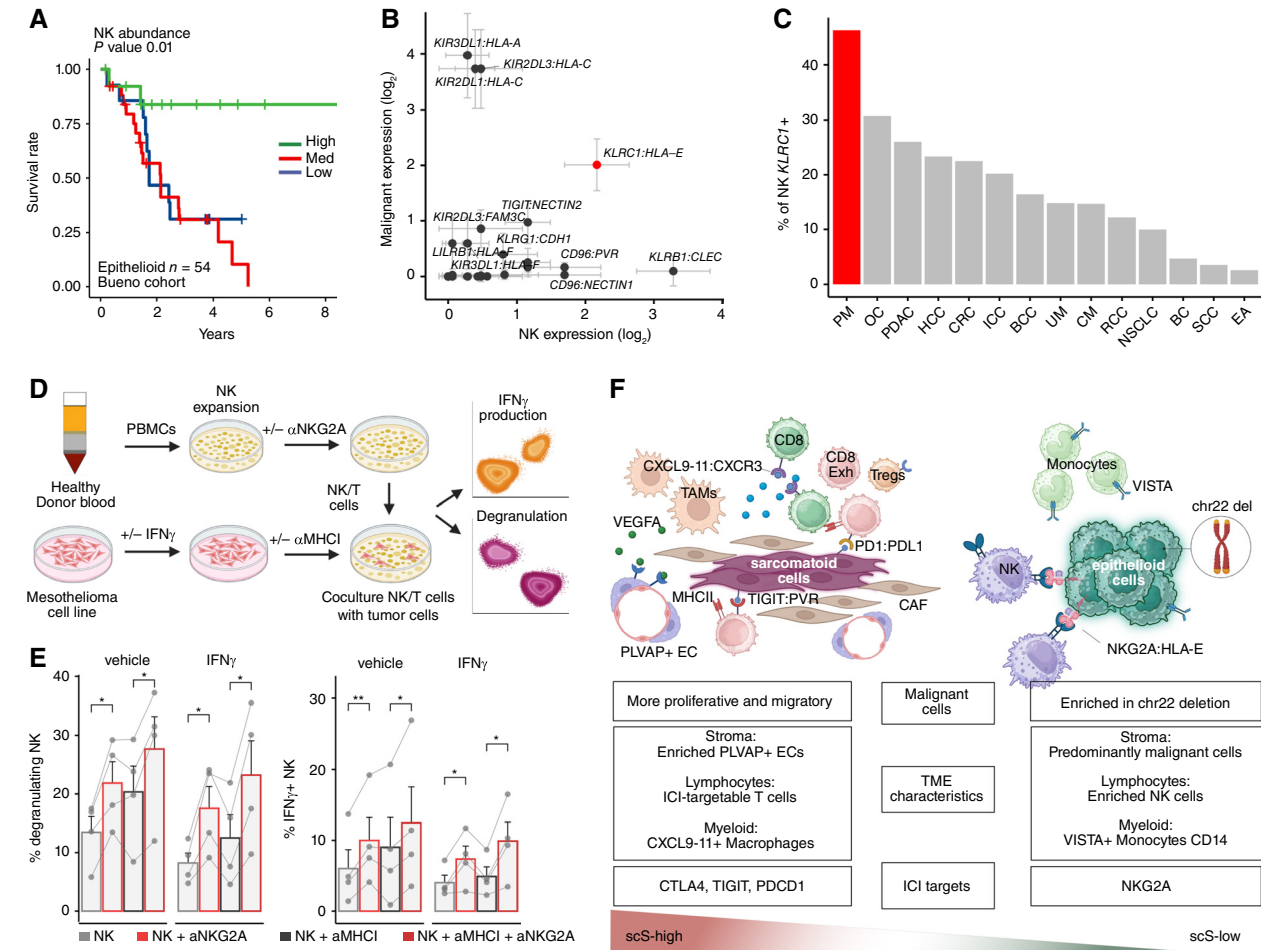


Figure 6. NK cell IC blockade targeting NKG2A as a novel therapeutic strategy in PM. **A**, Kaplan-Meier curve stratifying epithelioid samples in the Bueno cohort by NK cell abundance (deconvolved using BayesPrism). **B**, Log₂-normalized mean expression of ligand and receptors expressed by malignant cells (y axis) and NK cells (x axis), respectively. Error bars represent standard errors of expression across samples. **C**, Percentage of *KLRC1*-expressing NK cells averaged across patients with different cancer types combining scRNA-seq data from our and a pan-cancer study. **D**, Schematic of the coculture experimental design. **E**, Activation of NK cells cocultured with mesothelioma cell lines upon NKG2A blockade, indicated by degranulation (left) and IFN γ production (right) with or without anti-MHCI antibody and with or without IFN γ stimulation of PM cell lines. *P* values were computed using a paired Student *t* test. Error bars represent standard error. *, *P* < 0.05; **, *P* < 0.01; ***, *P* < 0.001; ****, *P* < 0.0001. **F**, Schematic of the key TME differences between scS-high and scS-low PM elucidated in our study (Created with BioRender.com). ICI = immune checkpoint inhibitor.

abundance in scS-high tumors. Further supporting this finding is a recent study employing spatial transcriptomics in PM biphasic samples, which showed increased lymphocytic infiltration and expression of chemokines CXCL9/10 in sarcomatoid-enriched regions (44). Future time-course studies will be needed to decipher the precise molecular events that trigger these highly divergent TMEs that track with the sarcomatoid–epithelioid axis.

Resolving the complexity of the immune–stroma–tumor interface and composition in the TME is of high clinical significance given that there are more than 4,700 immunotherapy agents in development (45), emphasizing the need for rational clinical trial design and patient treatment stratifications based on observations such as those reported here. Our data-driven approach highlighted an immunosuppressive NKG2A:HLA-E interaction between NK and tumor cells, which enhanced NK

cell activity upon NKG2A blockade in cocultures with PM cell lines. A previous study similarly reported the reactivity of NK cells isolated from PBMC of healthy individuals against mesothelioma cell lines when stimulated with IL15 (46). Further supported by the findings that *KLRC1* expression in NK cells is more abundant in PM relative to other cancer types and that NK cell content is an indicator of better overall survival in epithelioid PM, these initial results lay the ground for further investigations in experimental models of PM using anti-NKG2A therapeutics (e.g., monalizumab).

In conclusion, this study demonstrates the potential of high-throughput cellular profiling via scRNA-seq and in-depth analysis on PM clinical samples in identifying new cellular programs, prognostic signatures of disease outcome, and therapeutic targets toward the goal of achieving more effective, personalized therapies in PM.

Our study comes with several limitations. First, the small sample size of this rare cancer limited our ability to sample patients evenly across different molecular subtypes. Our analysis strived to overcome this limitation by corroborating our main findings using large bulk RNA-seq cohorts and performing associations between TME gene expression programs using rank statistics (Spearman correlation). However, this analytical approach, although robust to outliers, does not capture the absolute difference in amplitude of such molecular associations, and more sophisticated machine learning methods can be leveraged in the future with larger cohort sizes to model complex, nonlinear relationships between multiple cell-type-specific programs and the TME. Second, differences in TME along the sarcomatoid to epithelioid subtype gradient in our study were investigated using our *de novo*-identified scS-score, which is highly correlated with the sarcomatoid score from ref. 12 (Supplementary Fig. S2E). Nevertheless, other tumor-intrinsic transcriptional modules may emerge in future studies that could prove to be more informative in modeling the TME crosstalk in PM and stratifying patients for treatment. Indeed, a recent study employing bulk multimodal molecular profiling reported axes of molecular divergence orthogonal to the sarcomatoid score that impact patient survival and are driven by different levels of DNA methylation, genomic ploidy, and immune infiltration (10). Future efforts in characterizing the molecular aspects of PM should aim to leverage such multimodal technologies at single-cell resolution. Third, even though we were able to identify and validate the presence of a fetal-like, endothelial subpopulation, the stromal component in our scRNA-seq cohort was overall underrepresented, accounting for only 5,538 cells with several samples having very low numbers. This may have precluded us from uncovering additional stromal subpopulations of relevance for PM progression, especially among CAFs, that are known to be abundant in PM and contribute to its pathogenesis (47). Fourth, we capture 3,214 NK cells in our data that form three distinct populations; however, we anticipate that higher sampling of these cell types in PM and across cancer types will better inform on their functional diversity and therapeutic potential (bioRxiv 2023.10.26.564050). Lastly, our single-cell catalogue does not capture neutrophils, which are known to often escape detection in human samples utilizing the 10 \times Chromium scRNA-seq platform.

METHODS

Human Tumor Sample Collection

Tumor samples were obtained from diagnostic biopsies and surgical specimens of patients undergoing resection at Mount Sinai Hospital after obtaining written informed consent in accordance with a protocol reviewed and approved by the Institutional Review Board at the Icahn School of Medicine at Mount Sinai (IRB Human Subjects Electronic Research Applications 10-00472 and 10-00135), in collaboration with the Biorepository and Department of Pathology and conducted in accordance with the US Common Rule. Clinical information of participants can be found in Supplementary Table S1. Only patients with treatment-naïve PM were included in this study.

Tumor Sample Processing

Tumor samples were transported in MACS Tissue Storage Solution stored at 4°C, rinsed with PBS, minced, and incubated in a rotation shaker for 40 minutes at 37°C in collagenase IV 0.25 mg/mL, collagenase D 200 U/mL, and DNase I 0.1 mg/mL (all Sigma). Cell suspensions were then aspirated through a 18G needle 10 times and strained through a 70-micron mesh prior to RBC lysis. Dead cells were removed using a Dead Cell Removal Kit (Annexin V, Miltenyi Biotec). Cell suspensions were sorted into CD45 $^{+}$ and CD45 $^{-}$ cells using the EasySep Human CD45 Depletion Kit (Stem cell technologies) per kit instructions.

Tumor Single-Cell Library Construction and Sequencing

Single-cell RNA-seq (scRNA-seq) was performed at the Mount Sinai Genomics Core and Human Immune Monitoring Core on tumor samples using the Chromium platform (10 \times Genomics) with the 3' gene expression (3' GEX) V3 kit or 5' V2 kit. Approximately 4,000 CD45 $^{+}$ and 4,000 CD45 $^{-}$ cells were loaded into each channel of the 10 \times Chromium controller, following the manufacturer-supplied protocol. For 5' chemistry and the associated TCR V(D)J sequencing, 8,000 cells were targeted for recovery on each channel of the 10 \times Chromium X. 10 \times libraries were constructed using the 10 \times supplied protocol and sequenced at the Mount Sinai Genomics Core Facility. Gel bead in emulsions (GEM) were generated on the sample chip in the Chromium controller. Barcoded cDNA was extracted from the GEMs using Post GEM-RT Cleanup and amplified for 12 cycles. Amplified cDNA was fragmented and subjected to end-repair, poly-A-tailing, adaptor ligation, and 10 \times -specific sample indexing following the manufacturer's protocol. For TCR V(D)J-seq, a portion of the cDNA was also used to create targeted enrichment of the V(D)J sequences of the TCRs, following the manufacturer's instructions. Libraries were quantified using Bioanalyzer (Agilent) and QuBit (Thermo Fisher) analysis and then sequenced in single- or pair-end mode on a HiSeq 2500 or NovaSeq instrument (Illumina).

PBMC Sample Processing and Sequencing

PBMC sample processing and sequencing were performed at Immunai laboratories. PBMCs were isolated within 3 hours of collection via Ficoll density gradient centrifugation for 10 minutes at 1,200 g room temperature. The supernatant was then spun down at 500 g for 10 minutes at 4°C, and the pellet was resuspended to a concentration of 10 × 10 6 cells/mL cold Human Serum AB (GemCell HAB and HAB + 20% DMSO in 1:1 ratio). The resulting PBMCs were stored in 2-mL cryogenic vials in liquid nitrogen. For cell isolation, PBMCs were thawed, washed 2 \times in RPMI 2% FCS, treated with ACK lysis buffer (Lonza) to remove RBCs, and briefly incubated with DAPI. Approximately 300,000 cells were then sorted on a DAPI-negative gate. Cells were then stained for 30 minutes at room temperature with a panel of 138 Total-Seq-C antibodies [BioLegend, Stoeckius and colleagues (48)] and washed 3 \times using the HT1000 laminar wash system (Curox). Cells were then counted using the Cellaca MX High-throughput Automated Cell Counter as described in the manufacturer's protocol (Nexcelom), pooled, and loaded on the 10 \times Chromium 5 V2 and Next GEM Chip K Kit using a superloading strategy mixing cells from the same sample across lanes. BCR and TCR CDR3 sequences were enriched using the human V(D)J B-/T-cell enrichment. Libraries were prepared according to the manufacturer's protocol (10 \times Genomics) and sequenced on a NovaSeq 6000 System using the S4 2 \times 150 kit (Illumina). Raw reads were aligned to the human transcriptome using a splice-aware algorithm to produce cell-by-gene count matrices. Cells were separated to their respective samples using Seurat v4.4 built-in dehashing functions.

scRNA-seq Data Preprocessing, Quality Control, Clustering, Annotation, and Differential Expression

Single- (samples P2 and P9-P13) and pair-end (samples P1, P3, and P4-P8) FASTQ files were mapped to the GRCh38 human transcriptome using the count function in CellRanger > v3.1. Expression of

ambient RNA was mitigated using cellbender v0.3.0, and corrected count matrices were then normalized, log-transformed, and scaled using the Seurat v4.4 package in R. Cells with <400 genes, <1,000 unique molecular identifier (UMI) counts, or >25% mitochondrial gene expression detected were removed from downstream analyses. Principal component analysis and k-nearest neighbor (kNN) graphs were computed using Seurat default parameters. Based on the kNN graphs, a shared nearest neighbor graph was constructed to cluster cells with the original Louvain algorithm as implemented in Seurat. High-level cellular compartment annotations were assigned to clusters based on expressions of known cell class markers. For cell-type annotation of PBMC data, we used a reference-based method (<https://azimuth.hubmapconsortium.org/>). Doublet clusters were identified with higher-than-average gene and UMI counts, as well as expressions of markers from multiple high-level cellular compartment (e.g., CD45+ and CALB2+), and manually removed from downstream analyses. Data integration within each cell compartment was performed using harmony v0.1 to minimize sample-derived batch effects in aggregated visualizations. For batch effect correction across all cell compartments, scANVI model with n_layers = 3 and n_latent = 32 from scvi-tools v0.20.3 was used on raw counts to integrate the data across samples with default parameters when training. Differential expression analyses for *de novo* marker discovery were performed using Seurat FindMarkers function using a Wilcoxon rank sum test. Pathway and gene ontology analysis was carried out with clusterProfiler R package v4.6.0, using function enricher.

Defining Cell Programs Using cNMF

We applied nonnegative matrix factorization implemented in the Python package cNMF v1.3.4 to identify cellular states in each of the following cell types: malignant, endothelial, CAF, TAM, and T cells. For each, we tested from 5 to 30 K with 100 replicates and filtered outlier components with Euclidean distance >0.3 from their nearest neighbors. Then, based on the trade-off between reconstruction error and factorization stability and manual inspection of the modules, we selected the most appropriate Ks. We then computed cNMF module scores by taking the top 20 genes ranked by spectra scores for each cNMF module using Seurat function AddModuleScore. Prior to this, we removed gene redundancy in cNMF modules by assigning each gene to the cNMF module with the highest spectra score ensuring independence when computing module scores and pairwise correlation. To find associations between cNMF modules, we first computed the mean score for each cNMF module across cells of the relative compartment and then run pairwise Spearman correlations between cNMF modules across samples. For the fibroblasts and EC compartments, we computed cNMF modules from metacells computed using R package hdWGCNA v0.2.18, as these showed better performance compared with cNMF modules when using individual cells. We also merged cNMF modules whenever their expression was highly correlated across cells (taking the top 20 genes for each to compute a combined score) and removed others deemed to represent doublets, resulting in a total number of 54 cNMF that can be found in Supplementary Table S5.

Copy-Number Variations Inference

We used the package InferCNV v1.14.2 to infer CNA in the epithelial compartment of the scRNA-seq data. We used a set of normal distal lung cell types including normal mesothelial cells as reference (unpublished). We computed a CNA load score per cell by summing the absolute CNA scores per cell and then normalized the resulting values to the third quantile across cells per sample. A combination of the CNA load distribution and UMAP cell clustering of epithelial cells was used to identify true malignant cells. To infer genomic interaction with cancer cNMF modules, we applied the following strategy: (i) Metacells were computed using hdWGCNA function MetacellsByGroups ($k = 50$, max_shared = 30) excluding low cell number samples P1, P3 and P13.

(ii) We selected the most frequent CNA chromosomal rearrangements in our data (at regions: chr1p, chr3p, chr4, chr13, chr14, chr22), and queried all the genes contained in each chromosomal region using biomaRt v2.54.0, which were then used to compute a module score for each region and metacell. (iii) Malignant cNMF modules were recomputed on metacells, excluding all genes that overlapped selected genomic regions. (iv) The Spearman correlation was computed across metacells for each sample, and the median Spearman correlation coefficient was used for display in the heatmap in Fig. 1F. Similarly, for validating this analysis in the Bueno cohort, we took the average expression of the genes in each malignant cNMF module, excluding genes within a CNA region, and computed the Spearman correlation with the average expression of genes in each CNA region across samples.

Bulk RNA-Seq Datasets Acquisition and Analysis

RSEM-normalized count matrix including 82 bulk RNA-seq samples as part of the TCGA MESO cohort (Hmeljak cohort) was downloaded using the R package cgdsr v1.3 of cBioPortal (<http://www.cbioperl.org>), an online database built for cancer genomics along with metadata including histology information. The Bueno cohort was downloaded from the European Genome-phenome Archive under accession number EGAS00001001563 as RPKM-normalized count matrix including 216 bulk RNA-seq samples along with metadata information including histologic and molecular subtypes. Both datasets were \log_2 normalized before any downstream analysis. To compute the score for each scRNA-seq malignant cNMF program, we averaged the expression of the top 20 genes for each malignant cNMF module. For cNMF programs identified in other compartments, we first corrected the bulk normalized expression for a given cell-type abundance (e.g., T cells) by using the function removeBatchEffect from limma R package v3.54.0, in which we designated the expression of a canonical marker for a given cell type (e.g., CD3D for T cells) as a covariate. For immune content correction, we used the PTPRC marker gene, for T-cell infiltration, we used CD3D, and for endothelial content, we used VWF. This was done to ensure that differences observed in the bulk were not caused by higher or lower abundance of the cell compartment assessed. Additionally, to validate T-cell cNMF module enrichment across molecular subtypes, we selected most specific markers for each module: CD8A and CD8B for Tm2, HAVCR2 for Tm5, and FOXP3, TNFRSF18, and ILRA for Tm7. Similarly, we selected most specific marker genes for the fetal PLVAP⁺ EC subpopulation (ESM1, PLVAP, TP53I11, and INSR) to compute survival analysis.

Bulk RNA-seq Cell Type Deconvolution

Cell-type deconvolution of bulk RNA-seq samples was performed using the package BayesPrism v2.0. To identify significant differences in the deconvolved cell-type proportions, we calculated P values using the Dirichlet-multinomial regression analysis, implemented by the R package DirichletReg v0.7.1. Given that cell compositions sum to one, there is an inversely proportional relationship between cell fractions. Dirichlet-multinomial regression models these dependencies by accounting for the proportions of all other cell subsets when comparing the difference in one cell subset between two PM sample groups (e.g., difference in T cells between sarcomatoid and epithelioid molecular subtypes). Dirichlet regression was used to assess the significant variation in cell-type abundances from deconvolved bulk RNA cohorts and scRNA-seq data.

Assigning Bulk RNA-seq-Based Molecular Subtypes to Malignant Single Cells

Two-dimensional representation of PM subtypes in malignant cells was carried out similarly to Neftel and colleagues (49). Cells were first separated into sarcomatoid/biphasic-S versus epithelioid/biphasic-E by the sign of $D = \log_2 [\max(\text{sarcomatoid, biphasic-S}) - \max(\text{epithelioid, biphasic-E}) - 1]$, and D defined the y axis of all cells. For sarcomatoid/

biphasic-S cells (i.e., $D > 0$), the x axis value was defined as biphasic-S–sarcomatoid, and for epithelioid/biphasic-E cells (i.e., $D < 0$), the x axis was defined as epithelioid–biphasic-E.

Survival Analysis

We used a Kaplan–Meier (KM) model to estimate the survival function using the Bueno and Hmeljak cohorts, stratified by their expression levels of various gene modules that can serve as potential prognostic biomarkers. To adjust for histology or molecular subtype groups, we used a Cox proportional hazard regression model and computed P values. Both models were implemented using the survival v.3.4.0 R package. For Kaplan–Meier models, we grouped the samples into three groups based on their module score, with high assigned to the first quartile, medium (med) to the second and third quartile, and low to the fourth quartile. For Cox proportional hazard regression models we used both continuous and stratified expression values and relative P values were reported as P value (C) and P value (S), respectively. P values based on the log-rank test and the χ^2 test were used to determine the statistical significance of survival outcomes among the three groups in the Cox proportional hazard regression and KM models, respectively.

SCENIC Analysis

SCENIC v.1.1.2 was run using default settings on the myeloid, TAM, and ECs. With its implementation in R, SCENIC was run using the 500-bp and 10-kb motif databases for GENIE3 and RCisTarget. The regulon activity scores (AUC) were calculated using the AUCell v.4.2 R package for normal and fetal ECs using regulon information from the PM ECs.

NicheNet Analysis

We applied the NicheNet package v2.0.4 implemented in R to predict potential upstream ligands in the TMEs of specific gene signatures. The receiver was defined as the cell population most highly expressing a given module, and the sender was the other cell types. Background expressed genes were defined as the intersection of the top 5,000 variable features in the receiver cells and the ligand candidates in the ligand–target matrix database provided by NicheNet.

TCR-seq Analysis

TCR analysis was performed using R package scRepertoire v2.0. Filtered contig lists from each sample outputted from CellRanger were combined using the function CombineTCR and mapped to expression data via barcodes using the combineExpression function. Clonotypes were labeled as non-expanded, expanded small ($n > 1$ and $n \leq 5$, small), and expanded large ($n > 5$, large). To assess exhaustion in expanded clonotypes, we used the computed score for the exhaustion module Tm5 and averaged the score per clonotype across cells. For clonal overlap across samples and across sites, we used the “CTstrict” cloneall.

Quantification and Statistical Analyses

All statistical analyses are described in the figure legends. When multiple tests were performed, P values were corrected using the Benjamini–Hochberg procedure and false discovery rate (FDR) ≤ 0.05 . Significance annotation: *, $P < 0.05$; **, $P < 0.01$; ***, $P < 0.001$; and ****, $P < 0.0001$. P values > 0.05 are not shown.

Immunohistochemistry

Paraffin-embedded human mesothelioma tumor samples from all three histologic subtypes—epithelioid, biphasic, and sarcomatoid—as well as uninvolvled normal lung tissues from patients with lung adenocarcinoma, were sourced from the Biorepository Tissue Bank at the Icahn School of Medicine at Mount Sinai (ISMMS). These tissue samples were procured in accordance with protocols approved by the Institutional Review Board (IRB) of ISMMS. For IHC, 3 μ m sections

of these paraffin-embedded tissue sections were utilized. The IHC process was conducted at the Biorepository and Pathology Core at Mount Sinai using the VENTANA Discovery Ultra System (Roche) following the manufacturer's protocols. This involved de-paraffinization of the tissue sections, followed by sequential staining with primary antibody for CD31 (Roche) and PLVAP (Proteintech). Each primary antibody application was succeeded by the application of corresponding secondary antibodies—DISCOVERY OmniMap anti-Mouse HRP (RUO; catalog # 760-4310) and DISCOVERY Anti-Mouse HQ (catalog # 760-4814). The signals were then developed using different colors: the DISCOVERY ChromoMap DAB kit (RUO; catalog # 760-159) for brown and the DISCOVERY Purple kit (RUO; catalog # 760-229) for purple. After each staining phase, slides underwent a process of inhibition, heat denaturation, and neutralization. Subsequently, tissues were counterstained with hematoxylin to highlight the nuclei in blue. The stained sections were imaged using NanoZoomer S60 Digital slide scanner (Hamamatsu), and the acquired images were analyzed using the HALO Image Analysis Platform (Indica Labs). CD31+ vessels, characterized by brown-stained particles in the cytoplasm, were quantified. Simultaneously, PLVAP-positive cells, discerned by purple-stained particles, were identified. The percentage of CD31 and PLVAP double-positive ECs within blood vessels was then calculated for graphical representation. For each sample, quantification was conducted on 9 to 23 randomly selected regions of interest (ROI). Statistical significance of the findings was assessed using a paired Student t test.

Immunophenotyping of Mesothelioma Cell Lines and NK Cells

We performed immunophenotyping on all four mesothelioma cell lines used in this study: NCI-H28 (ATCC CRL-5820), MSTO-211H (ATCC CRL-2081), NCI-H2052 (ATCC CRL-5915), and NCI-H2452 (ATCC CRL-5946). The cell lines were cultured in RPMI1640 medium (ATCC, #30-2001) supplemented with 10% FBS and penicillin/streptomycin and incubated at 37°C with 5% CO₂. These cell lines were sourced from ATCC, which conducts regular short-tandem repeat genotyping and *Mycoplasma* testing. Additionally, the cells were maintained in culture for a duration of less than 6 months from the time of resuscitation. Experimental procedures were conducted within eight passages from the initial frozen stocks. Each cell line was treated overnight in fully supplemented RPMI medium, either with or without 200 ng/mL recombinant human interferon gamma (rhIFN γ). Following treatment, cells were stained with Zombie NIR (BioLegend) for viability assessment. Subsequently, Fc blocking was performed using TruStain FcX, and the cells were stained with HLA-E PE antibody (BioLegend) to assess the surface expression of these receptors. The comprehensive analysis of receptor expression was conducted using flow cytometry with a Cytek Aurora system. PBMC were isolated from healthy donor's blood using density gradient centrifugation with Lymphoprep (STEMCELL Technologies) as the separation medium. The freshly isolated PBMCs were subsequently cultured in human NK MACS medium (Miltenyi Biotec) for 2 to 3 weeks to ensure optimal *in vitro* expansion of NK cells. NK cells were analyzed by flow cytometry for expression of NKG2A using the abovementioned protocol but with anti-human NKG2A PECy5 antibody (BioLegend).

Mesothelioma-NK Cell Coculture Assay

Mesothelioma cell lines were prepared by incubation with or without 200 ng/mL rhIFN γ in fully supplemented RPMI medium overnight. For the coculture assay, mesothelioma cell lines were further pretreated with anti-MHC class I antibody (10 μ g/mL; Clone W6/32, BioLegend) for 1 hour, whereas human blood-derived *in vitro* expanded NK cells were pretreated with anti-NKG2A (10 μ g/mL; Beckman Coulter) antibody for 1 hour. Subsequently, NK and mesothelioma cells were combined in a 96-well plate at an effector to target (E:T) ratio of 6:1. Anti-CD107a-BV785 antibody (BioLegend) at 1:500 dilution was added to the cells. After 1 hour, the culture was supplemented with

0.5× concentrations of both brefeldin A and monensin (BioLegend) to facilitate cytokine retention within the cells. The cocultured cells were then incubated for a total of 16 hours. Post-incubation, the cells underwent staining with Zombie NIR (BioLegend) for viability assessment, Fc blocked using TruStain FcX, and then stained with surface antibodies, including CD45 BUV395, CD3 BUV496, CD4 BV570, CD8 PerCP Cy5.5, CD56 BUV805, PD1 BV711, and NKG2A PECy5 (BioLegend). The cells were fixed using IC fixation buffer (BioLegend) and intracellularly stained using granzyme A AF700 and IFN γ PE antibodies in 1× permeabilization buffer (BioLegend). Finally, the stained samples were subjected to flow cytometric analysis using a Cytek Aurora system to quantitatively assess NK cell degranulation and cytokine production. FlowJo was used for flow cytometry data analysis. We employed the Flow AI algorithm via the FlowJo software platform. This approach facilitated the automated identification and exclusion of aberrant events, ensuring high-quality data for subsequent analysis. The parameters and thresholds for Flow AI were set in accordance with the software's guidelines to optimize data integrity and analytic accuracy.

Graphical Illustrations

Graphical elements used to create experimental design schemes were created with a paid licensed version of BioRender.

Data Availability

Raw scRNA-seq, CITE-seq, and TCR-seq data along with processed files have been deposited in the Gene Expression Omnibus (<https://www.ncbi.nlm.nih.gov/geo/>) and are available under accession number: GSE190597. The rest of the data was queried from publicly available repositories. The Hmeljak cohort (8) and the full bulk RNA-seq TCGA cancer cohort were obtained through cBioPortal (<http://www.cbiportal.org>). The Bueno cohort (9) was downloaded from the European Genome-phenome Archive under accession number EGAS00001001563. The human adult lung atlas scRNA data (22) was downloaded from <https://www.synapse.org/#!Synapse:syn21041850/wiki/600865>. The human fetal lung atlas scRNA data (23) was downloaded from <https://fetal-lung.cellgeni.sanger.ac.uk/scRNA.html>. The immune pan-cancer scRNA study (38) was downloaded from <https://zenodo.org/records/5186413/#%20.YRqbJC1h2v6>. Code to reproduce computational analyses results can be accessed at https://github.com/TsankovLab/PM_scRNA_atlas.

Authors' Disclosures

S. Gnjatic reports grants from Regeneron, Boehringer-Ingelheim, Takeda, Celgene, Janssen R&D, and BMS and personal fees from Taiho outside the submitted work. R.P. Sebra reports personal fees from GeneDx and other support from Panacent Bio outside the submitted work. A. Horowitz reports grants from AstraZeneca outside the submitted work. T.U. Marron reports grants and personal fees from Regeneron and Merck, personal fees from EMD Serono, Astellas, Arcus, AbbVie, Ono, Fate, Avimmune, Geneos, and BMS, and personal fees from AstraZeneca outside the submitted work. A.M. Tsankov reports grants from Immunai during the conduct of the study. No disclosures were reported by the other authors.

Authors' Contributions

B. Giotti: Formal analysis, investigation, methodology, data curation, writing-original draft, visualization, software. **K. Dolasia:** Investigation, validation, formal analysis, data curation, methodology, writing-original draft, visualization. **W. Zhao:** Investigation, methodology, resources, software. **P. Cai:** Formal analysis, investigation, software, writing-original draft. **R. Sweeney:** Investigation, resources. **E. Merritt:** Validation, writing-review and editing. **E. Kiner:** Resources, writing-review and editing. **G.S. Kim:** Formal analysis, software. **A. Bhagwat:** Formal analysis, software, data curation. **T. Nguyen:** Formal analysis. **S. Hegde:** Formal analysis, writing-review and editing.

B.G. Fitzgerald: Resources, writing-review and editing. **S. Shroff:** Resources. **T. Dawson:** Resources. **M. Garcia-Barros:** Resources, validation. **J. Abdul-Ghafar:** Resources. **R. Chen:** Resources. **S. Gnjatic:** Resources. **A. Soto:** Resources. **R. Brody:** Resources, validation. **S. Kim-Schulze:** Resources. **Z. Chen:** Resources, writing-review and editing. **K.G. Beaumont:** Resources. **M. Merad:** Resources. **R.M. Flores:** Resources. **R.P. Sebra:** Resources, writing-review and editing. **A. Horowitz:** Methodology, supervision. **T.U. Marron:** Resources, writing-review and editing. **A. Tocheva:** Methodology, resources, supervision, validation, writing-review and editing. **A. Wolf:** Resources. **A.M. Tsankov:** Conceptualization, funding acquisition, supervision, project administration, formal analysis, investigation, methodology, data curation, resources, software, validation, visualization, writing-review and editing, writing-original draft.

Acknowledgments

We thank all members of the ISMMS Genomics Core, Human Immune Monitoring Core, and Immunai that helped with single-cell profiling and sequencing of tumor and blood samples, respectively. This research was also conducted with support from the Biorepository and Pathology Core at Mount Sinai. This work was supported in part by the American Association for Thoracic Surgery/Women in Thoracic Surgery Mid-career Investigator Grant for A. Wolf and Immunai and ISMMS seed funding for A.M. Tsankov.

Note

Supplementary data for this article are available at Cancer Discovery Online (<http://cancerdiscovery.aacrjournals.org/>).

Received January 12, 2023; revised March 24, 2024; accepted July 2, 2024; published first July 3, 2024.

REFERENCES

1. Selikoff IJ, Churg J, Hammond EC. Relation between exposure to asbestos and mesothelioma. *N Engl J Med* 1965;272:560–5.
2. Huang J, Chan SC, Pang WS, Chow SH, Lok V, Zhang L, et al. Global incidence, risk factors, and temporal trends of mesothelioma: a population-based study. *J Thorac Oncol* 2023;18:792–802.
3. Koopmans T, Rinkevich Y. Mesothelial to mesenchyme transition as a major developmental and pathological player in trunk organs and their cavities. *Commun Biol* 2018;1:170.
4. Vogelzang NJ, Rusthoven JJ, Symanowski J, Denham C, Kaukel E, Ruffie P, et al. Phase III study of pemetrexed in combination with cisplatin versus cisplatin alone in patients with malignant pleural mesothelioma. *J Clin Oncol* 2003;21:2636–44.
5. Zalcman G, Mazieres J, Margery J, Greillier L, Audigier-Valette C, Moro-Sibilot D, et al. Bevacizumab for newly diagnosed pleural mesothelioma in the Mesothelioma Avastin Cisplatin Pemetrexed Study (MAPS): a randomised, controlled, open-label, phase 3 trial. *Lancet* 2016;387:1405–14.
6. Baas P, Scherpereel A, Nowak AK, Fujimoto N, Peters S, Tsao AS, et al. First-line nivolumab plus ipilimumab in unresectable malignant pleural mesothelioma (CheckMate 743): a multicentre, randomised, open-label, phase 3 trial. *Lancet* 2021;397:375–86.
7. Desai A, Garrison T, Rose B, Tan Y, Hill B, Pemberton E, et al. OA08.03 phase II trial of pembrolizumab (NCT02399371) in previously-treated malignant mesothelioma (MM): final analysis. *J Thorac Oncol* 2018;13:S339.
8. Hmeljak J, Sanchez-Vega F, Hadley KA, Shih J, Stewart C, Heiman D, et al. Integrative molecular characterization of malignant pleural mesothelioma. *Cancer Discov* 2018;8:1548–65.
9. Bueno R, Stawiski EW, Goldstein LD, Durinck S, De Rienzo A, Modrusan Z, et al. Comprehensive genomic analysis of malignant pleural mesothelioma identifies recurrent mutations, gene fusions and splicing alterations. *Nat Genet* 2016;48:407–16.

10. Mangiante L, Alcalá N, Sexton-Oates A, DiGenova A, Gonzalez-Perez A, Khandekar A, et al. Multiomic analysis of malignant pleural mesothelioma identifies molecular axes and specialized tumor profiles driving intertumor heterogeneity. *Nat Genet* 2023;55:607–18.
11. Alcalá N, Mangiante L, Le-Stang N, Gustafson CE, Boyault S, Damiola F, et al. Redefining malignant pleural mesothelioma types as a continuum uncovers immune-vascular interactions. *EBioMedicine* 2019;48:191–202.
12. Blum Y, Meiller C, Quetel L, Elarouci N, Ayadi M, Tashtanbaeva D, et al. Dissecting heterogeneity in malignant pleural mesothelioma through histo-molecular gradients for clinical applications. *Nat Commun* 2019;10:1333.
13. Lee H-S, Jang H-J, Choi JM, Zhang J, de Rosen VL, Wheeler TM, et al. Comprehensive immunoproteogenomic analyses of malignant pleural mesothelioma. *JCI Insight* 2018;3:e98575.
14. Gonzalez Castro LN, Tirosh I, Suva ML. Decoding cancer biology one cell at a time. *Cancer Discov* 2021;11:960–70.
15. Bou-Samra P, Chang A, Azari F, Kennedy G, Segil A, Guo E, et al. Epidemiological, therapeutic, and survival trends in malignant pleural mesothelioma: a review of the National Cancer Database. *Cancer Med* 2023;12:12208–20.
16. Hillen H, Candi A, Vanderhoydonck B, Kowalczyk W, Sansores-Garcia L, Kesikciadou EC, et al. A novel irreversible TEAD inhibitor, SWTX-143, blocks hippo pathway transcriptional output and causes tumor regression in preclinical mesothelioma models. *Mol Cancer Ther* 2024;23:3–13.
17. Park S, Schalling M, Bernard A, Maheswaran S, Shipley GC, Roberts D, et al. The Wilms tumour gene WT1 is expressed in murine mesoderm-derived tissues and mutated in a human mesothelioma. *Nat Genet* 1993;4:415–20.
18. Yang ZY, Yang X, Xu S, Jin P, Li XT, Wei X, et al. Reprogramming of stromal fibroblasts by SNAI2 contributes to tumor desmoplasia and ovarian cancer progression. *Mol Cancer* 2017;16:163.
19. Hylebos M, Van Camp G, Vandeweyer G, Fransen E, Beyens M, Cornelissen R, et al. Large-scale copy number analysis reveals variations in genes not previously associated with malignant pleural mesothelioma. *Oncotarget* 2017;8:113673–86.
20. Longhitano L, Forte S, Orlando L, Grasso S, Barbato A, Vicario N, et al. The crosstalk between GPR81/IGFBP6 promotes breast cancer progression by modulating lactate metabolism and oxidative stress. *Antioxidants (Basel)* 2022;11:275.
21. Yamaguchi T, Hayashi M, Ida L, Yamamoto M, Lu C, Kajino T, et al. ROR1-CAVIN3 interaction required for caveolae-dependent endocytosis and pro-survival signaling in lung adenocarcinoma. *Oncogene* 2019;38:5142–57.
22. Travaglini KJ, Nabhan AN, Penland L, Sinha R, Gillich A, Sit RV, et al. A molecular cell atlas of the human lung from single-cell RNA sequencing. *Nature* 2020;587:619–25.
23. He P, Lim K, Sun D, Pett JP, Jeng Q, Polanski K, et al. A human fetal lung cell atlas uncovers proximal-distal gradients of differentiation and key regulators of epithelial fates. *Cell* 2022;185:4841–60.e25.
24. Sharma A, Seow JJW, Dutertre C-A, Pai R, Blériot C, Mishra A, et al. Onco-fetal reprogramming of endothelial cells drives immunosuppressive macrophages in hepatocellular carcinoma. *Cell* 2020;183:377–94.e21.
25. Wei G, Srinivasan R, Cantemir-Stone CZ, Sharma SM, Santhanam R, Weinstein M, et al. Ets1 and Ets2 are required for endothelial cell survival during embryonic angiogenesis. *Blood* 2009;114:1123–30.
26. Lin Q, Lu J, Yanagisawa H, Webb R, Lyons GE, Richardson JA, et al. Requirement of the MADS-box transcription factor MEF2C for vascular development. *Development* 1998;125:4565–74.
27. Oda N, Abe M, Sato Y. ETS-1 converts endothelial cells to the angiogenic phenotype by inducing the expression of matrix metalloproteinases and integrin beta3. *J Cell Physiol* 1999;178:121–32.
28. Lines JL, Pantazi E, Mak J, Sempere LF, Wang L, O'Connell S, et al. VISTA is an immune checkpoint molecule for human T cells. *Cancer Res* 2014;74:1924–32.
29. Andersson A, Yang S-C, Huang M, Zhu L, Kar UK, Batra RK, et al. IL-7 promotes CXCR3 ligand-dependent T cell antitumor reactivity in lung cancer. *J Immunol* 2009;182:6951–8.
30. Harlin H, Meng Y, Peterson AC, Zha Y, Tretiakova M, Slingluff C, et al. Chemokine expression in melanoma metastases associated with CD8⁺ T-cell recruitment. *Cancer Res* 2009;69:3077–85.
31. Sichien D, Scott CL, Martens L, Vanderkerken M, Van Gassen S, Plantinga M, et al. IRF8 transcription factor controls survival and function of terminally differentiated conventional and plasmacytoid dendritic cells, respectively. *Immunity* 2016;45:626–40.
32. Lehtonen A, Matikainen S, Julkunen I. Interferons up-regulate STAT1, STAT2, and IRF family transcription factor gene expression in human peripheral blood mononuclear cells and macrophages. *J Immunol* 1997;159:794–803.
33. Osuna-Gómez R, Arquerol C, Galano C, Mulet M, Zamora C, Barnadas A, et al. Effector mechanisms of CD8⁺ HLA-DR⁺ T cells in breast cancer patients who respond to neoadjuvant chemotherapy. *Cancers (Basel)* 2021;13:6167.
34. Horiuchi S, Wu H, Liu WC, Schmitt N, Provost J, Liu Y, et al. Tox2 is required for the maintenance of GC T_{FH} cells and the generation of memory T_{FH} cells. *Sci Adv* 2021;7:eabj1249.
35. Mannarino L, Paracchini L, Pezzuto F, Olteanu GE, Moracci L, Vedovelli L, et al. Epithelioid pleural mesothelioma is characterized by tertiary lymphoid structures in long survivors: results from the MATCH study. *Int J Mol Sci* 2022;23:5786.
36. Liu B, Hu X, Feng K, Gao R, Xue Z, Zhang S, et al. Temporal single-cell tracing reveals clonal revival and expansion of precursor exhausted T cells during anti-PD-1 therapy in lung cancer. *Nat Cancer* 2022;3:108–21.
37. André P, Denis C, Soulas C, Bourbon-Caillet C, Lopez J, Arnoux T, et al. Anti-NKG2A mAb is a checkpoint inhibitor that promotes anti-tumor immunity by unleashing both T and NK cells. *Cell* 2018;175:1731–43.e13.
38. Nieto P, Elosua-Bayes M, Trincado JL, Marchese D, Massoni-Badosa R, Salvany M, et al. A single-cell tumor immune atlas for precision oncology. *Genome Res* 2021;31:1913–26.
39. Ferrara N, Adamis AP. Ten years of anti-vascular endothelial growth factor therapy. *Nat Rev Drug Discov* 2016;15:385–403.
40. Garcia J, Hurwitz HI, Sandler AB, Miles D, Coleman RL, Deurloo R, et al. Bevacizumab (Avastin) in cancer treatment: a review of 15 years of clinical experience and future outlook. *Cancer Treat Rev* 2020;86:102017.
41. Chia PL, Russell P, Asadi K, Thapa B, Gebski V, Murone C, et al. Analysis of angiogenesis and stromal biomarkers in a large malignant mesothelioma cohort. *Lung Cancer* 2020;150:1–8.
42. Yu D, Walker LSK, Liu Z, Linterman MA, Li Z. Targeting T_{FH} cells in human diseases and vaccination: rationale and practice. *Nat Immunol* 2022;23:1157–68.
43. Fridman WH, Meylan M, Petitprez F, Sun C-M, Italiano A, Sautès-Fridman C. B cells and tertiary lymphoid structures as determinants of tumour immune contexture and clinical outcome. *Nat Rev Clin Oncol* 2022;19:441–57.
44. Torricelli F, Donati B, Reggiani F, Manicardi V, Piana S, Valli R, et al. Spatially resolved, high-dimensional transcriptomics sorts out the evolution of biphasic malignant pleural mesothelioma: new paradigms for immunotherapy. *Mol Cancer* 2023;22:114.
45. Upadhyaya S, Hubbard-Lucey VM, Yu JX. Immuno-oncology drug development forges on despite COVID-19. *Nat Rev Drug Discov* 2020;19:751–2.
46. Sottile R, Tannazzi M, Johansson MH, Cristiani CM, Calabro L, Ventura V, et al. NK- and T-cell subsets in malignant mesothelioma patients: baseline pattern and changes in the context of anti-CTLA-4 therapy. *Int J Cancer* 2019;145:2238–48.
47. Chrisochoidou Y, Roy R, Farahmand P, Gonzalez G, Doig J, Krasny L, et al. Crosstalk with lung fibroblasts shapes the growth and therapeutic response of mesothelioma cells. *Cell Death Dis* 2023;14:725.
48. Stoeckius M, Hafemeister C, Stephenson W, Houck-Loomis B, Chattopadhyay PK, Swerdlow H, et al. Simultaneous epitope and transcriptome measurement in single cells. *Nat Methods* 2017;14:865–8.
49. Neftel C, Laffy J, Filbin MG, Hara T, Shore ME, Rahme GJ, et al. An integrative model of cellular states, plasticity, and genetics for glioblastoma. *Cell* 2019;178:835–49.e21.